

AN ABSTRACT OF THE THESIS OF

C. Christopher Chickadel for the degree of Master of Science in Oceanography
presented on August 23, 2002.

Title: Measuring Surface Longshore Currents with an Optical Technique
Redacted for Privacy

Abstract approved: _____
Robert A. Holman

Longshore currents are frequently occurring phenomena capable of transporting beach sediments, causing accretion and erosion of the shoreline. Forcing mechanisms are understood and well modeled for cases of alongshore homogeneous and monotonic bathymetry, yet the extension of these models to complex and irregular bathymetry sometimes fails. To test and improve these models, observational data over large spatial and temporal scales and from a variety of beaches and forcing conditions is necessary. *In situ* instruments have the drawback of being costly and difficult to operate for very long periods (months to years) over wide areas (hundreds of meters) on a routine basis, due to the frequent care and attention they demand while in the high energy environment of the surf zone.

We present an optical method (Optical Current Meter or OCM) to measure the longshore component of surface currents in the nearshore by measuring the alongshore drift of persistent sea foam in the surf zone. The method is based on short time series of video data collected from an alongshore array of pixels. These

space-time data are first Fourier transformed to a frequency-wavenumber spectrum, and finally to a velocity spectrum. A model of the velocity spectrum, including energy from noise and the expected energy from drifting foam traces, is fitted to the observed spectrum to estimate the foam drift velocity. The 95% confidence interval around the velocity estimate and other measures of the input and output data quality are calculated.

Tests with synthetic data were performed to evaluate the ability of the OCM to measure the mean current in the presence of waves and wave orbital velocity contamination. Synthetic tests showed that, over a range of mean velocities, orbital velocities, and varying time series lengths used in the analysis, the OCM accurately estimated the mean current (with maximum RMS error of 0.033 m/s for an 8 s window of analysis).

Approximately one month of video data from the 1997 SandyDuck field experiment was collected from an alongshore array of pixels collocated in the video image with an *in situ* bidirectional electromagnetic current meter, and was used to ground truth test the OCM. Mean longshore currents were estimated from each instrument for overlapping data records. The root-mean-square error between the two records is 0.11 m/s. Additionally, a linear regression showed the gain between the two instruments to not be statistically different from one. The differences between the surface and interior measurements were compared to forcing mechanisms that may cause surface velocity shear. A linear regression of surface

velocity shear to alongshore wind stress was well correlated for cases when waves were arriving from the south with no significant correlation for waves arriving from the north. We attribute this to an increased sensitivity to misregistration errors when viewing waves from the north. This technique can be applied to study large-scale coastal behavior and to measure shear waves of longshore currents.

©Copyright by C. Christopher Chickadel
August 23, 2002
All Rights Reserved

Measuring Surface Longshore Currents with an Optical Technique

by
C. Christopher Chickadel

A THESIS

submitted to
Oregon State University

in partial fulfillment of
the requirements for the
degree of

Master of Science

Presented August 23, 2002
Commencement June 2003

Master of Science thesis of C. Christopher Chickadel presented on August 23, 2002

APPROVED:

Redacted for Privacy

Major Professor, representing Oceanography

Redacted for Privacy

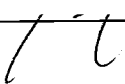
Dean of the College of Oceanic and Atmospheric Sciences

Redacted for Privacy

Dean of the Graduate School

I understand that my thesis will become part of the permanent collection of Oregon State University libraries. My signature below authorizes release of my thesis to any reader upon request.

Redacted for Privacy

 C. Christopher Chickadel, Author

ACKNOWLEDGEMENTS

From my summers spent on the New Jersey shore as a child, I developed a love of the beach, sand, waves and water. From my time doing this research, I have developed an appreciation for all the questions there are to be answered about what goes on at that wild place where waves meet sand. I would like to first thank Rob Holman for giving me the chance to “push back the frontiers of science” and help to answer some of those questions, if only a small bit of it. Thank you to my committee members Mike Freilich, for his initial work on the OCM method and comments, and Paul Komar for his editorial comments.

I would also like to thank all the members of the CIL, past and present, students research assistants and undergraduates for all of their help, encouragement and laughs along the way. In particular, thanks to Joe for allowing me to get to the beach, John for keeping the world in balance and making the wheels of scientific research move, Nathaniel for providing code and explanations (and a house) when I was stuck, and Hilary for all her advice and science questions, even from Florida. Thanks to Drew, James and Cindy for their invaluable perspectives on science and family.

Thank you to my family who has always encouraged me to do what I wanted and need to do, and provided me with the love and support to do just that. And last, but not least, I owe a lot to Deborah, the love of my life, for coming along

for the ride to Corvallis and graduate school. It's been fun, it's been hard, and we've even increased the size of our family by 50% (yea Gilly! I love you too).

This research was funded by the Office of Naval Research grant # N00014-96-10237. In situ longshore current and pressure sensor measurements were courteously provided by Steve Elgar and Robert Guza. Wave direction and wind measurements were collected and processed by the staff and researchers at the USACE Field Research Facility.

TABLE OF CONTENTS

	<u>Page</u>
Chapter 1: Introduction	1
1.1 Longshore Sediment Transport	5
1.2 Modeling of Longshore Currents	6
1.2.1 Oblique wave approach	9
1.2.2 Longshore pressure gradient	11
1.2.3 Wind forcing	12
1.3 Measurements of Longshore Currents	15
1.4 Objectives	16
Chapter 2: Optical Current Meter Technique	18
2.1 Video Data Collection	18
2.1.1 Argus video monitoring stations	18
2.1.2 Pixel time series collection	20
2.2 OCM Algorithm	23
2.2.1 $S(f, k_y)$ calculation	24
2.2.2 $S(v, k_y)$ transformation	26
2.2.3 $S(v)$ transformation	28
2.2.4 $S(v)$ model	30
2.2.5 Velocity estimate quality	32
2.2.6 Viewing angle velocity bias	33
2.2.7 Generating a time series	37
2.3 Synthetic Data Tests	37
2.3.1 Synthetic timestacks	37
2.3.2 Mean current estimation	38
2.3.3 Results	41
2.3.4 Velocity bias due to aliasing	45

TABLE OF CONTENTS (Continued)

	<u>Page</u>
Chapter 3: Field Test	48
3.1 Introduction	48
3.2 <i>In Situ</i> Data	49
3.3 Video Data	53
3.3.1 Collection	53
3.3.2 OCM processing	55
3.3.3 Wave breaking filter	58
3.4 Ground Truth Test Results	58
3.5 Analysis of Vertical Shear in the Upper Water Column	68
Chapter 4: Discussion	73
Chapter 5: Conclusions	79
Bibliography	82

LIST OF FIGURES

<u>Figure</u>	<u>Page</u>
1.1 Cross-shore schematic of the nearshore system based on fluid dynamics (after Komar, 1998).....	2
1.2 An idealized longshore current velocity profile representing wave driven models and observations	3
1.3 The Indian River Inlet, Delaware looking north in the direction of the dominant littoral transport (<i>photo courtesy Tony Dalrymple</i>).....	7
2.1 Snapshot taken by the Argus Station at Duck NC.....	19
2.2 Snapshot of the surfzone at Duck NC (top panel).....	22
2.3 Frequency-wavenumber spectrum of the timestack in Figure 2.2.....	25
2.4 $S(v, k_y)$ spectrum shows a concentration of energy at about 0.6 m/s in wavenumber-velocity space.....	27
2.5 $S(v)$ spectrum derived from Figure 2.4.....	29
2.6 The sample histogram from a 32 s section of a timestack shows a broad range of image intensity.....	34
2.7 Synthetic stack examples.....	39
2.8 The results from the synthetic stack test of the OCM for various window lengths, T_l	42
2.9 Total root-mean-square error for each window length, T_l , over all mean velocities and maximum orbital velocities.....	43
2.10 The results from the synthetic stack test of the OCM for various wave periods and constant window length, $T_l = 32$ s.	44

LIST OF FIGURES (Continued)

<u>Figure</u>	<u>Page</u>
2.11 Total root-mean-square error for each wave period for all mean velocities and orbital velocity amplitudes.....	46
3.1 Plan view of the collocated current meters and pressure sensors, bathymetry and OCM pixel array.....	51
3.2 A camera view of the longshore pixel array (oblique line) used for the field test.....	54
3.3 Sample timestack (left panel) with superimposed progressive vector diagram (PVD) and longshore current time series (right panel).....	56
3.4 A section of a timestack, on the left, taken on Oct. 2 at 1534 GMT.....	57
3.5 The same stack from Figure 3.3, with the contaminated middle section removed (left panel).....	59
3.6 I_{range} variable compared with the absolute deviation of surface currents from interior longshore currents.....	60
3.7 Fifteen sample surface (solid lines) and interior (dashed lines) longshore current time series.....	62
3.8 Optically measured mean surface currents ('o') and <i>in situ</i> currents ('x') for October and the first week of November, 1997, at Duck NC.....	63
3.9 <i>In situ</i> longshore current means, \bar{v}_i , versus surface longshore current means, \bar{v}_s	64
3.10 Probability density plot of the difference between mean surface and interior longshore currents, v_{diff}	66
3.11 v_{diff} compared to the alongshore component of wind stress....	67

LIST OF FIGURES (Continued)

<u>Figure</u>	<u>Page</u>
3.12 v_{diff} compared to the estimated alongshore component of wave roller stress.....	69
4.1 A cross-shore OCM array designed to measure the mean cross-shore profile of the longshore current (upper panel).....	75
4.2 IMLE spectrum (lower panel) produced from a three hour record of longshore current velocity from the shear wave array (top panels).....	78

Measuring Surface Longshore Currents with an Optical Technique

Chapter 1: Introduction

Komar (1998) defines the nearshore region as the area of ocean from the shoreline to just beyond the region of breaking waves (Figure 1.1), which is characterized by complex and energetic water motions. Waves shoal and break over bathymetric features, transferring momentum to the water column through turbulent dissipation of the wave energy forcing fluid circulation and currents, including longshore currents. The action of currents and waves has the ability to transport sediment, altering the bathymetric features of the nearshore region, and in turn influencing wave shoaling and fluid flow.

Within the nearshore region we define the longshore current as the narrow band of water flow parallel and adjacent to the shoreline (Figure 1.2). The longshore current is substantially contained within the surf zone, where velocity magnitudes are small at the shoreline, maximum near the maximum of wave dissipation and decrease offshore, in the case of a plane sloping beach with no offshore bar. With a bar present there is often a peak in the flow velocity near the bar crest and another peak near the shore (Symonds and Huntley, 1980). The vertical structure of the longshore current flow is nearly depth uniform, except at the bed where it decreases rapidly to zero. Time averaged velocities of the

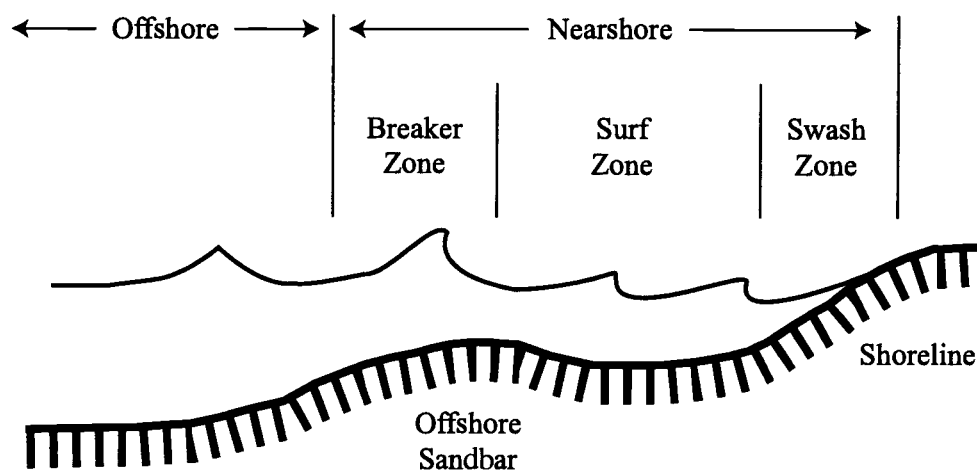


Figure 1.1 Cross-shore schematic of the nearshore system based on fluid dynamics (after Komar, 1998).

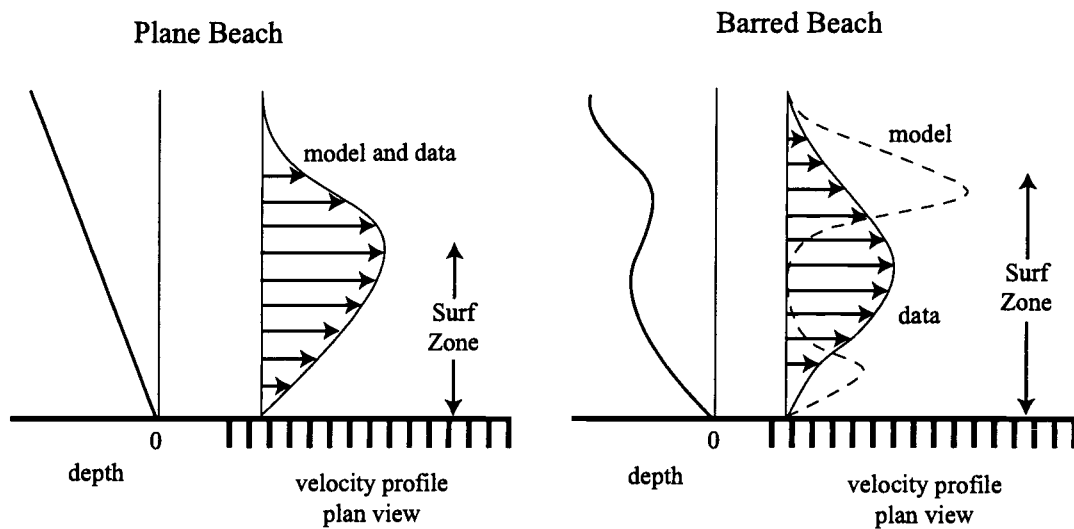


Figure 1.2 An idealized longshore current velocity profile representing wave driven models and observations. The left panel illustrated the case for a plane beach where observational data of the longshore current generally match model outputs, while in the right panel, illustrating a beach with an offshore sandbar, data were often contrary to the modeled longshore current profile, as explained in §1.2.

longshore current have been measured to be near 2 m/s during storm conditions with more energetic pulses (Oltman-Shay *et al.*, 1989).

Longshore transport of sediment by waves and currents, and particularly divergences in that transport, are perhaps the primary mechanism for long term erosion and accretion of beaches is the. Since longshore sediment transport is driven by longshore currents, a predictive understanding of this phenomenon requires an understanding of longshore currents. While the theory of longshore current generation is well developed and has been used to model data from specific cases (Tornton and Guza, 1986), their application to the more common complex nearshore morphologies has been very limited. More complex models exist, yet the observational data with which to test them is lacking. Quantitative observations of the nearshore flow field over wide spatial coverage and for long time periods are needed.

In this context we introduce an optically based method to measure surface longshore currents based on the time/space drift of longshore advected residual sea foam. This technique can provide an extensive database with the necessary temporal and spatial coverage. This chapter focuses on a discussion of our motivation, including the impact of longshore currents on sediment transport, contemporary theory on longshore current dynamics, and the availability of longshore current measurements. We conclude with our objectives for the

development and testing of our optical current meter technique.

1.1 Longshore Sediment Transport

Longshore currents, combined with waves, provide the driving mechanism for the alongshore transport of sand. Strong cross-shore flows produced by wave action set sediment into motion to be carried by longshore currents along the beach. The resulting net littoral drift, moving hundreds of thousands of cubic meters of sand per year (Komar, 1998), accounts for most of the erosion and accretion along the shoreline.

We define a right-hand Cartesian coordinate system with x positive in the offshore direction, z positive upward and y oriented in the alongshore direction. If we define the sea bed as $z = Z$, then we can describe erosion and accretion, using conservation of mass, as

$$\frac{dZ}{dt} = -\frac{1}{\kappa} \left(\frac{\partial Q_y}{\partial y} + \frac{\partial Q_x}{\partial x} \right) \quad (1)$$

where Q is the transport of sand with components Q_x and Q_y , and κ is a packing factor. When man made structures, such as jetties and breakwaters or natural landforms, such as rocky headlands, interfere with the longshore transport of sediments a strong gradient in Q_y is created driving erosion and accretion. This phenomenon is evident in the observation of accretionary wedges of sand and

sediments at the up-current side of groynes, jetties, breakwaters and headlands, and loss of sand, or erosion, on the down-current side (Figure 1.3).

Coastal regions in the U.S. and around the world are often economically dependent on their beaches, so have the most to lose to beach erosion. Strategies for managing beach erosion includes the construction of groynes, and the like, and sand replenishment (Corps of Engineers, 1971), often without quantitative knowledge of the natural patterns of longshore currents and the resulting littoral drift. This can be costly or even disastrous, as unexpected erosion and accretion can occur which then must be remedied by further construction and beach nourishments (Goss, 2002). Simple monitoring of the pattern and temporal variability of longshore currents could help to construct jetties and groynes more effectively and to plan efficient beach nourishments.

1.2 Modeling of Longshore Currents

The present section reviews forcing mechanisms for longshore currents based on the alongshore momentum balance. The equations of motion for time-averaged flows are the depth integrated shallow-water nonlinear momentum equations (e.g. Mei, 1989)

$$\rho(\bar{\eta} + h) \left(\frac{\partial \bar{u}}{\partial t} + \bar{u} \frac{\partial \bar{u}}{\partial x} + \bar{v} \frac{\partial \bar{u}}{\partial y} \right) = -\rho g(\bar{\eta} + h) \frac{\partial \bar{\eta}}{\partial x} - \left(\frac{\partial S_{xx}}{\partial x} + \frac{\partial S_{yx}}{\partial y} \right) - \tau_x^{bed} + \tau_x^{wind} - F_x \quad (2a)$$

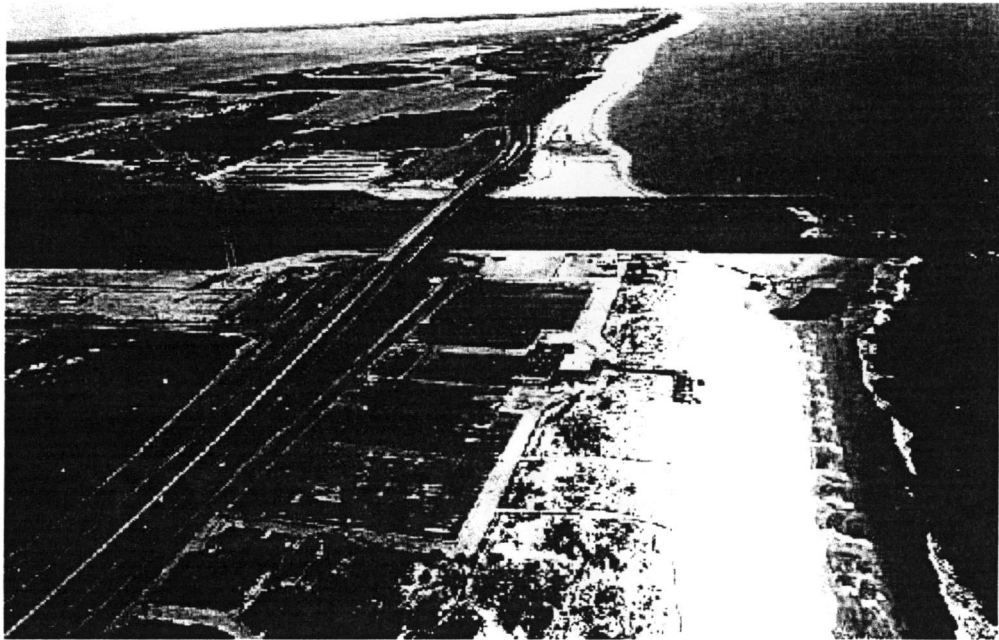


Figure 1.3 The Indian River Inlet, Delaware looking north in the direction of the dominant littoral transport (*photo courtesy Tony Dalrymple*).

and

$$\rho(\bar{\eta} + h) \left(\frac{\partial \bar{v}}{\partial t} + \bar{u} \frac{\partial \bar{v}}{\partial x} + \bar{v} \frac{\partial \bar{v}}{\partial y} \right) = -\rho g(\bar{\eta} + h) \frac{\partial \bar{\eta}}{\partial y} - \left(\frac{\partial S_{xy}}{\partial x} + \frac{\partial S_{yy}}{\partial y} \right) - \tau_y^{bed} + \tau_y^{wind} - F_y. \quad (2b)$$

Water density is ρ , η is the free surface displacement, h is the still water depth, u and v are the cross-shore and alongshore components of fluid velocity, respectively. S is the radiation stress tensor describing the mean flux of momentum associated with organized wave motions (Longuet-Higgins and Stewart, 1964). The additional terms in (2) include the bed stress τ^{bed} , wind stress τ^{wind} , and mean turbulent momentum flux terms F which describe momentum mixing. Overbars indicate time-averaged quantities, over many wave periods. For waves approaching a straight beach from angle α , the terms of the radiation stress tensor are given by

$$S = \begin{bmatrix} S_{xx} & S_{xy} \\ S_{yx} & S_{yy} \end{bmatrix} = \frac{1}{8} \rho g H^2 \begin{bmatrix} \frac{kh(\cos^2(\alpha) + 1)}{\sinh 2kh} - \frac{1}{2} & \frac{kh \sin(2\alpha)}{2 \sinh 2kh} \\ \frac{kh \sin(2\alpha)}{2 \sinh 2kh} & \frac{kh(\sin^2(\alpha) + 1)}{\sinh 2kh} - \frac{1}{2} \end{bmatrix} \quad (3)$$

where k is wavenumber and H is wave height. Equation (2) contains three driving terms for longshore currents: a direct forcing by obliquely-approaching waves, a secondary forcing by longshore pressure gradients and direct wind forcing. These are represented by the second, first and third terms on the right hand side of (2b) and will be discussed below.

1.2.1 Oblique wave approach

The primary mechanism for the generation of longshore currents is thought to be due to the oblique approach of breaking waves. Bowen (1969a) and Longuet-Higgins (1970a, 1970b) were the first to derive an analytic formulation for wave driven longshore currents by balancing the cross-shore gradient of the cross-shore flux of longshore directed momentum, denoted by the radiation stress term, S_{xy} , with frictional drag on the bed to force longshore currents. This can be derived from (2) by assuming steady state conditions, uniform in the alongshore direction, with no flow through the shoreline and no wind, yielding

$$\frac{\partial S_{xy}}{\partial x} + \tau_y^{bed} = -F_y. \quad (4)$$

The frictional drag component at the sea bed, τ_y^{bed} , can be modeled as a linear drag law (Longuet-Higgins, 1970a)

$$\tau_y^{bed} = \frac{2}{\pi} C_f \rho u_m \bar{v} \quad (5)$$

where C_f is the frictional drag coefficient, u_m is the maximum horizontal wave orbital velocity and \bar{v} is the time averaged longshore current velocity. Assuming monochromatic waves, plane sloping bathymetry and no horizontal mixing we can solve for \bar{v} . Predicted currents rise from zero near the shoreline to a maximum at the break point and drop to zero outside the break point. By increasing the mixing

term, F_y , a smoother cross-shore profile of longshore current can be obtained.

Thornton and Guza (1986) took a different approach in trying to model the cross-shore profile of the longshore current. They studied the case of random wave field with wave heights described by a Rayleigh distribution and transformed the distribution as the waves broke across the surf zone (Thornton and Guza, 1983). Because waves of different heights break at different depths, the input of momentum due to breaking waves is naturally distributed in the cross-shore yielding a smooth forcing function with no discontinuities. This eliminates the need for a horizontal mixing term, and the modeled output agrees well with longshore velocity data collected at the 1980 Nearshore Sediment Transport Study (Thornton and Guza, 1986).

While purely wave driven models predict the existence of longshore currents on plane sloping beaches well, quantitative discrepancies arise when they are applied to beaches having sandbars, as was found at the 1990 DELILAH field experiment in Duck, North Carolina (Birkemeier, 1997). The main disagreement is that the idealized models predict two longshore current maxima, one near the shore and a larger maximum at the bar crest, while the data usually indicate a single current maximum, typically located at the position of the trough (schematically shown in Figure 1.2). Models have been developed to account for these unexpected observations of the cross-shore profile of the mean longshore current. These

include hypothesized increased mixing due to shear waves (Church *et al.*, 1992; Özkan-Haller and Kirby, 1997), landward shifts due to the influence of wave rollers (Lippmann *et al.*, 1994) and changes due to the role of local pressure gradients (Reneirs, 1999).

1.2.2 Longshore pressure gradient

Beaches often exhibit longshore variability in the underlying bathymetry and in wave heights. These variations can lead to longshore pressure gradients that may also force a longshore current. Using the equations of motion (2b) and assuming weak alongshore variations, Putrevu and others (1995) derived a simple expression for the alongshore momentum balance including waves and alongshore pressure gradients

$$F_y = -\rho g(\bar{\eta} + h) \frac{\partial \bar{\eta}}{\partial y} - \frac{\partial S_{xy}}{\partial x} - \tau_y^{bed}. \quad (6)$$

An alongshore sloping water surface, $\partial \bar{\eta} / \partial y$, is thought to be derived mainly from alongshore differences in the wave set-up, the super elevation of sea level that balances cross-shore gradients in S_{xx} across the surf zone (from 2a, Bowen, 1969b)

$$\frac{\partial S_{xx}}{\partial x} + \rho g(\bar{\eta} + h) \frac{\partial \bar{\eta}}{\partial x} = 0. \quad (7)$$

Alongshore setup variations arise from non-uniform alongshore beach

bathymetry, or alongshore variations in wave height, or both. These can cause alongshore pressure gradients, driving longshore currents from areas of large waves and high wave set-up to areas of smaller waves and lower set-up. If alternating regions of high and low wave set-up exist, alongshore cell circulation will usually result, with alternating areas of divergence and convergence of alongshore directed currents (Bowen, 1969b). Narrow regions of swift offshore flow, rip currents, exist in areas of converging longshore currents, and diffuse flow toward shore is observed at areas of divergence.

Reiners (1999) examined the possibility of alongshore pressure gradients causing the discrepancy between oblique wave forcing models and observed currents on barred beaches. He used numerical models to reproduce conditions typical during the DELILAH field experiment and found that bathymetry-induced longshore pressure gradients were probably present and could account for the observed location of a longshore current maximum in the trough.

1.2.3 Wind forcing

Wind is a well known forcing mechanism for the circulation of the world's oceans (Monk, 1950). Wind blowing over the surface of the water produces a frictional stress in the direction of the wind velocity, driving waves and currents. The basic formulation for wind and wave induced currents in the nearshore is taken from equation (2b) assuming uniformity in the alongshore direction and steady state

conditions

$$\tau_y^{wind} = \tau_y^{bed} \quad (8)$$

where alongshore wind stress, τ_y^{wind} , is modeled as a quadratic drag law (Taylor, 1916)

$$\tau_y^{wind} = C_d \rho_a |w| w_y \quad (9)$$

and C_d is the drag coefficient, ρ_a is the density of air, w is the wind velocity and w_y is the longshore component of that velocity, usually measured at an elevation of 10 m above sea level.

The role of wind in forcing longshore currents in the nearshore has been mostly neglected, due to the prevailing view that wave generated currents dominate in the surf zone, and because the simultaneous generation of both currents and waves by wind forcing presents difficulties in observing the two phenomena separately. It is not clear how to distinguish currents driven directly by the wind stress versus those driven by breaking waves simultaneously forced by the same wind stress.

Whitford and Thornton (1993) examined the surf zone-wide integrated longshore currents using a model of the alongshore momentum balance including wave and wind forcing, and assuming uniform bathymetry and forcing in the

alongshore direction. For a planar beach, their model showed that total wind forcing over the surf zone was proportional to the surf zone width, and hence was inversely proportional to the beach slope. Most importantly, they showed that for some conditions (gently sloping beaches and strong alongshore winds) wind forcing can be of the same order as wave forcing. These model results compared favorably with wind, wave and longshore current data collected from Duck, NC during 1986.

Fedderson and others (1998) obtained similar results to the previous authors when numerically modeling the longshore currents generated by wind and waves using data from the 1997 SandyDuck field experiment. The authors compared the combination of wind and wave forcing to the calculated bottom stress integrated across the entire nearshore region. Generally, they found that wind stress is a statistically significant forcing factor accounting for about one third of the total longshore current forcing. Secondly, they found that the integrated surf zone currents (where waves are actively breaking) correlated best with wave forcing alone, while outside of the surf zone wind accounted for the majority of longshore current forcing.

Beyond these studies little has been done to quantify the degree to which wind forces longshore currents. In particular, there is little knowledge about the depth dependent shear induced by wind stress, as all of the previous nearshore studies dealt only with *in situ* current meters that are required to be submerged to

make a measurement, so can never be placed close to a potential surface shear layer. It remains largely undetermined whether or not there is an observable depth current shear due to wind forcing in surf zone flows.

1.3 Measurements of Longshore Currents

Because nearshore flow fields often exhibit large spatial variations, sampling arrays must be spatially extensive and dense. Such arrays have been deployed in the past, during intensive field experiments such as NSTS (Guza and Thornton, 1980; Thornton and Guza, 1986) and during several of the Duck field experiments (e.g. DELLAH, SandyDuck). However, these represent a few, focused efforts. *In situ* arrays are simply too expensive to maintain. In the surf zone strong oscillatory flows and turbulence due to breaking and shoaling waves can easily damage or tear *in situ* current meters from their moorings. Sediment, biofouling and drifting aquatic vegetation carried by longshore currents and wave action, can clog and generally interfere with most types of *in situ* current meters, demanding frequent care and attention. Furthermore, installation and alignment is difficult in an active surf zone. Thornton and Guza (1986) found most of these difficulties present when conducting a field data collection at Leadbetter Beach, CA, as part of the Nearshore Sediment Transport Study, where nearly half of their current meters were damaged during the course of a three week experiment.

In response to these difficulties, the design of instrument arrays for most

field experiments has involved compromises. Arrays are usually placed in a cross-shore or an alongshore orientation, often with the assumptions of longshore homogeneity. Array design is usually optimized around an initial bathymetry in hopes that the future bathymetry and fluid flow patterns remain relatively stationary for the duration of a lengthy experiment. Movement of a large array of instruments, once installed, is nearly impossible. It is clear that *in situ* instruments are invaluable for focus experiments of limited size, spatially and temporally, but an adaptable long term data gathering system is needed.

In this paper we describe an alternative approach, an optical current meter for the long term measurement of longshore currents. It is based on Argus stations, inexpensive permanent optical systems operational at a variety of beach sites around the world (Holman et al., 1993). Argus stations are able to collect data over many time scales (tenths of a second to years) and spatial scales (meters to kilometers). Additionally, this remote sensing system offers the ease of adapting to changing conditions that is not possible with almost all *in situ* instruments.

1.4 Objectives

The primary objective of this study is to develop and field test an optically based method to measure surface longshore currents. This method will exploit the naturally present drifting sea foam left after the passage of breaking waves. An optical method, using video cameras, has many benefits over the typical *in situ*

current meter. With video cameras a large region of interest can be studied with a dense spatial sampling. Data can be collected for extended periods since a camera's installation life time is typically many years. Installation and care of a video system is straight forward and relatively inexpensive. On the other hand, the method will be limited to regions of wave breaking, may provide gappy time series, and may be sensitive to winds. The relationship of a surface-following technique to a mid-water column measure of the longshore current will have to be tested.

The first step in development of our current meter demonstrates the abilities of our optical current meter using synthetic data, for which we can control all aspects of the input data. The second step, presented as a separate chapter in this thesis, presents field tests of our optical current meter through comparisons with a collocated *in situ* current meter. Finally, the relationship between misfits of surface measurements to mid-water measurements will be explored.

Chapter 2: Optical Current Meter Technique

Optical techniques to measure fluid velocities, such as Particle Image Velocimetry (PIV), are not new. All methods rely on tracking patterns, or particles, in two-dimensional space to determine particle velocities and thereby infer the velocities of the surrounding region. In the surf zone, residual sea foam left from passing breaking waves provides useful particle drifters (Figure 2.1), indicating the magnitude and direction of the prevailing surface current. However, traditional PIV methods require large computational effort and appear sensitive to tracking the bore front of breaking waves. We have developed an alternative method to measure longshore currents from video, based on the time-space characteristics of foam traces from an alongshore-oriented transect of image pixels. Individual foam traces are not used, instead the bulk frequency-longshore wavenumber spectrum of a sample time-space window is analyzed.

2.1 Video Data Collection

2.1.1 Argus video monitoring stations

The nearshore environment exhibits a range of visible signatures from which important signals can be estimated (Holman *et al.*, 1993). The period and direction of breaking waves can be measured (Lippmann and Holman, 1991). Runup time series can be measured from the variable wet edge of the shoreline that

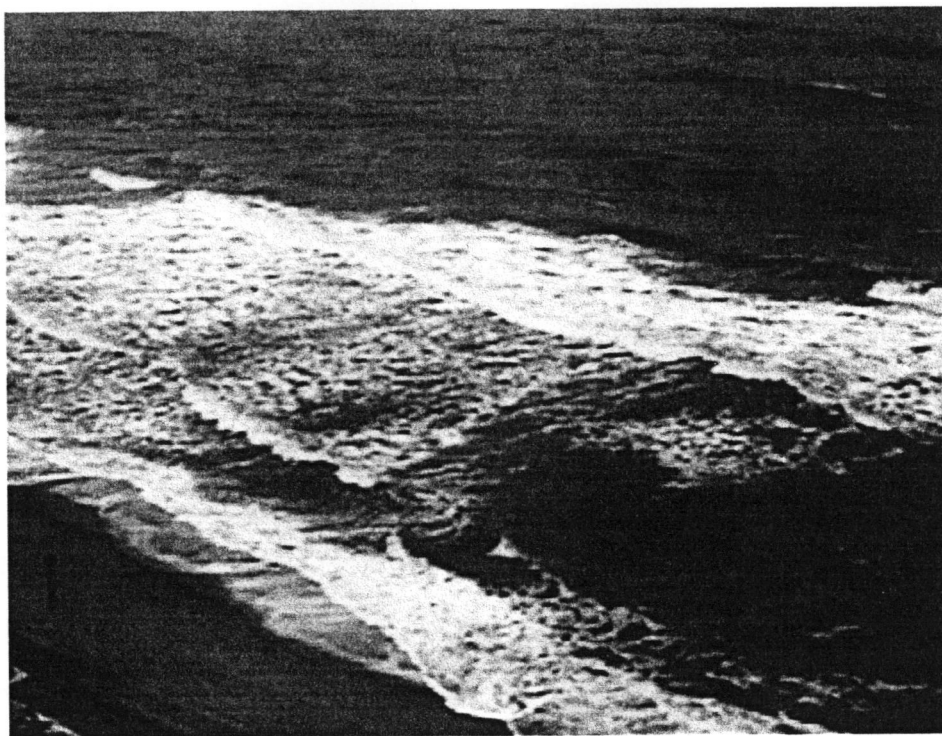


Figure 2.1 Snapshot taken by the Argus Station at Duck NC. The image details the range of characteristic foam patch sizes. For scale, the circular target in the lower left is approximately 0.5 meters in diameter.

is the swash zone (Holland and Holman, 1993). This potential led to the development of unmanned video monitoring platforms called Argus Stations (Holman et al., 1993). Each Argus station consists of a computer programmed to automatically collect and process video images from a small number of commercially available video cameras (usually two to six). Each camera, mounted to view the beach from an oblique aerial view, surveys a different portion of the beach, so the entire area of interest is covered by a combination of the camera views. Image data collection is automatic according to a user-defined schedule. Data transfer back to a central data server via internet or phone line usually occurs nightly or hourly.

2.1.2 Pixel time series collection

Quantification of the image data relies on the transformation from a two dimensional image plane to three dimensional real world coordinates. Remote sensing using aerial photography and satellite imagery is not a new concept (Wolf and Dewitt, 2000), and the problem has received much attention. Holland and others (1997) determined a geometrical solution for image to real world transformation for video monitoring of the nearshore environment. This technique uses the measured real world location of the camera and the measured location of at least two ground control points (GCPs: real world objects within the camera's view, whose world coordinates are known) to solve for the unknown camera parameters:

roll, tilt, azimuth and field of view. Given these known parameters and the camera's real world location it is possible to solve for the image coordinates (u,v) of points in the real world (x,y,z) . Sampling arrays are designed in real world space with transformation to pixel coordinates and distribution of sampling among cameras invisible to the user.

The video data from which we determine alongshore surface velocities is collected from an alongshore oriented array of pixels (Figure 2.2). A pixel is the individual unit of a video image. The resolution of a pixel, ε , can be roughly determined by the formula

$$\varepsilon \approx 2R \tan \frac{\delta}{2} \quad (10)$$

where δ is the radial field of view subtended by each pixel, and R is the distance from the camera to the object being viewed. We have chosen our pixel array to have a resolution of 0.25 m, and to be 30 m in length, to adequately resolve the typical range of foam patch sizes, which we have determined through inspection, to be 1 to 10 m.

Once the position and size of the pixel array was determined, video data, time series of pixel intensity on a 256 level gray scale, from each pixel in the alongshore array are digitally recorded by the image processing computer. The data are recorded at 2 Hz sampling (15 frame increments) from each of the pixel

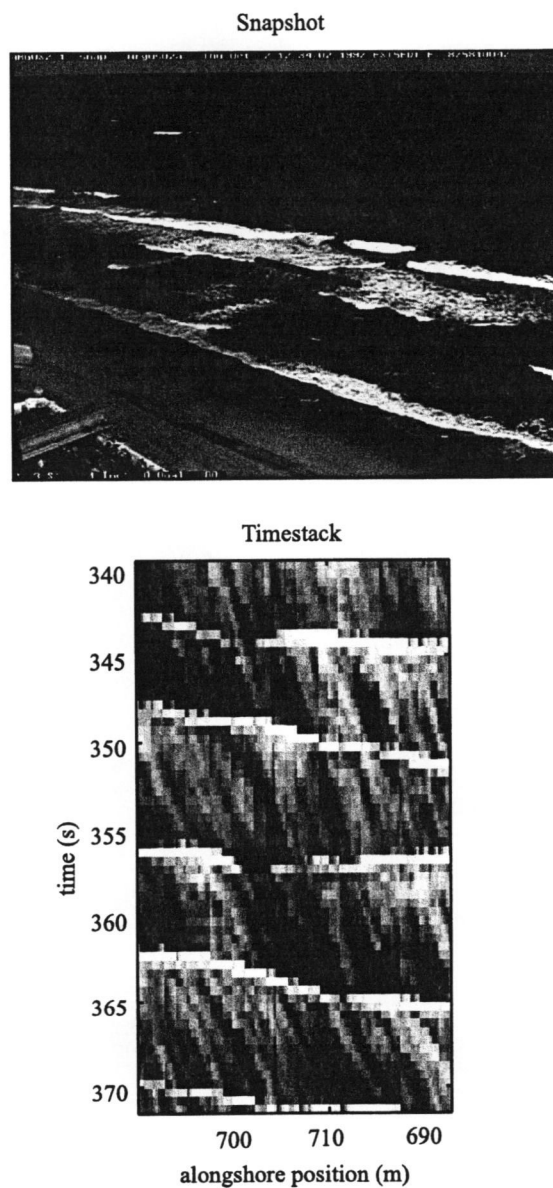


Figure 2.2 Snapshot of the surfzone at Duck NC (top panel). The line indicates the location of an alongshore pixel array where the video record, called a *timestack*, was taken (bottom panel). The timestack reveals the bright horizontal bands of passing breaking waves and the oblique traces of foam patches drifting with the prevailing longshore current.

locations comprising the video instrument. The composite view of video data returned from the array arranged in chronological order vertically, is called a *timestack*, as seen in Figure 2.2.

2.2 OCM Algorithm

In this section we outline the signal processing steps needed to transform the video measurements of surface foam drift to an estimate of surface longshore currents. Our objectives are to develop a straightforward and relatively simple technique that produces an accurate estimate of the magnitude and direction of the mean surface longshore current for the length of window of analysis along with an estimate of the error. In addition, objective criteria will be developed and tested to identify data segments for which no useful estimation can be made.

The algorithm consists of four steps: computation of a two dimensional frequency-wavenumber spectrum; transformation of the spectrum into a wavenumber-velocity spectrum; integration through wavenumber to produce a velocity spectrum (the distribution of image intensity variance with estimated velocity); and finally estimation of a single most representative velocity for that segment. The sample video data being analyzed is the section of timestack shown in Figure 2.2.

2.2.1 $S(f, k_y)$ calculation

The initial step is to transform the video data, $I(t, y; x)$, from a space, x and y , and time, t , domain to a frequency-wavenumber domain using a two dimensional Fourier transform $\hat{I}(f, k_y; x)$. The analytical form of this transformation is

$$\hat{I}(f, k_y; x) = \iint B(t, y) I(t, y; x) e^{-i2\pi ft} e^{-i2\pi k_y y} dt dy \quad (11)$$

where f is frequency and k_y is alongshore wavenumber. The data are simultaneously windowed with a two dimensional Bartlett multiplicative filter, $B(t, y)$, (Press et al., 1992) to reduce smearing and leakage in the spectrum. The two-dimensional spectrum, $S(f, k_y)$, is computed as

$$S(f, k_y) = \hat{I}(f, k_y) \hat{I}(f, k_y)^* \quad (12)$$

where the asterisk (*) denotes the complex conjugate. Figure 2.3 shows the spectrum, $S(f, k_y)$, of the sample timestack from Figure 2.2. Features in the original timestack image have analogs in the spectrum. The horizontally oriented bright bands in the time series are caused by passing breaking waves and appear in the f - k_y spectrum as energy aligned along the zero wavenumber axis (the abscissa in Figure 2.3). Since y -directed or longshore velocity is the ratio of frequency to wavenumber we can recognize that lines of constant velocity are represented as rays extending from the origin of the spectrum, with slope inversely proportional to velocity. Negative velocities are associated with negative frequencies, and positive velocities

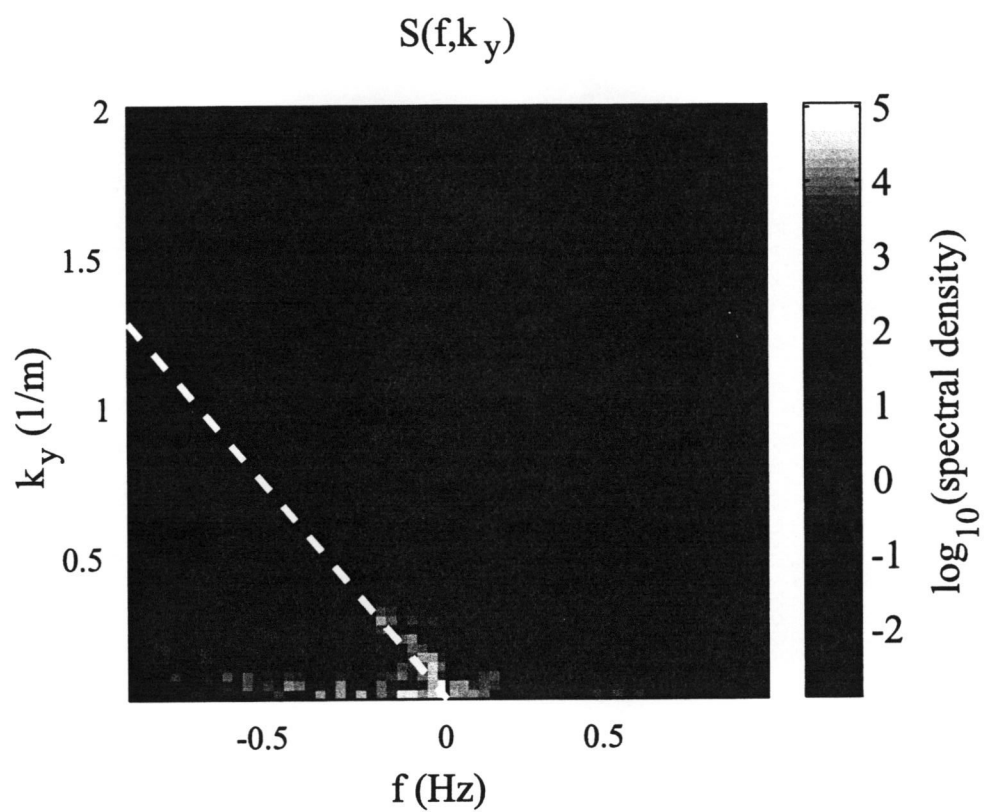


Figure 2.3 Frequency-wavenumber spectrum of the timestack in Figure 2.2. Note the concentration of energy along the dashed line indicating the constant velocity line of -1 m/s.

with positive frequencies. Because residual foam in the surf zone has a broad distribution of characteristic wavelengths, the energy representing the oblique traces of foam streaks should then lie generally along one of these lines, extending through many wavenumbers and frequencies, if the surface longshore speed was consistent in space and time.

2.2.2 $S(v, k_y)$ transformation

The spectrum is then transformed from frequency-wavenumber space to velocity- wavenumber space. We use the mapping $v = f/k_y$ to make our transformation to velocity space-wavenumber, but we wish to conserve variance in our transformation so that

$$\begin{aligned} \text{var}\{S(f, k_y)\} &= \iint S(f, k_y) df dk_y \\ &= \iint S(v, k_y) |k| dv dk_y \end{aligned} \quad (13)$$

where $|k|$ is the Jacobian determinant and $S(v, k_y)$ is the velocity-wavenumber spectrum. To eliminate possible contamination resulting from obliquely incident waves which mimic rapidly moving sea foam, the velocity range is constrained to lie between ± 3 m/s. The alongshore projection of wave speed for an oblique wave is usually well out of this range while longshore currents are typically within this range. The resulting spectrum, $S(v, k_y)$ (Figure 2.4), indicates a lobe of energy due to the oblique traces of drifting foam within this velocity confined region. The

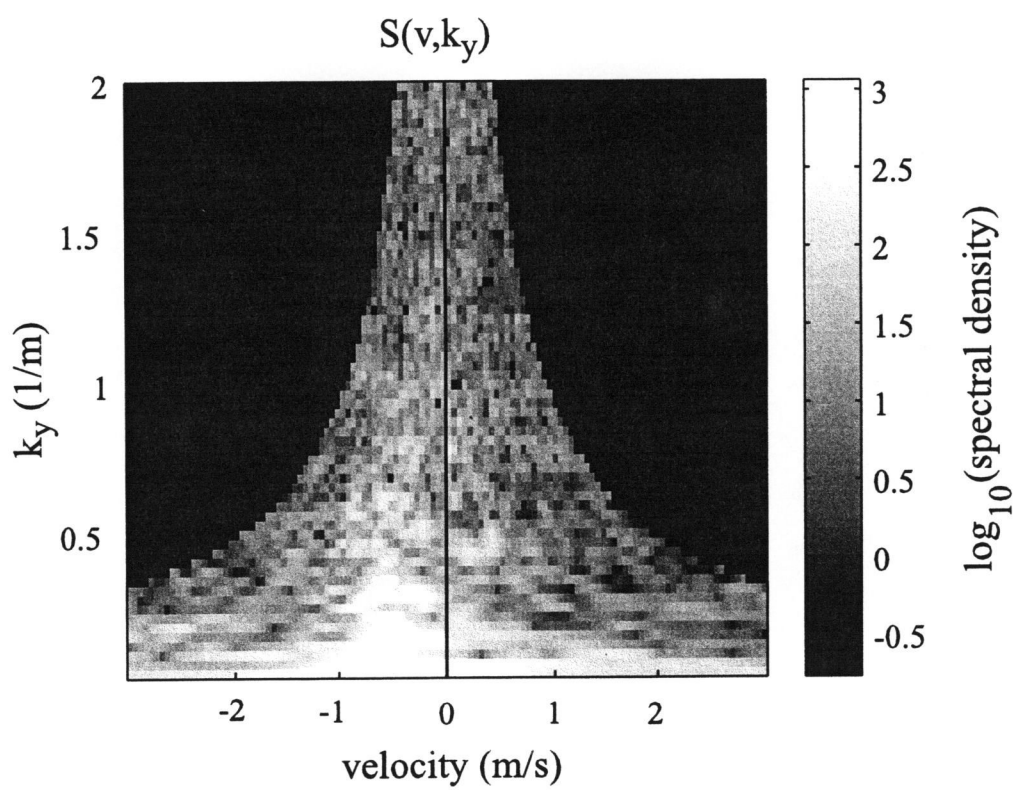


Figure 2.4 $S(v, k_y)$ spectrum shows a concentration of energy at about 0.6 m/s in wavenumber-velocity space.

regions of no data in the velocity extremes at higher wavenumbers are due to the extension of our mapping bounds beyond the original $S(f, k_y)$ spectrum (beyond the Nyquist frequency).

2.2.3 $S(v)$ transformation

The $S(v, k_y)$ spectrum can be further simplified to $S(v)$ by integrating with respect to wavenumber, with the region of no data treated as zero energy content

$$S(v) = \int_{k_{min}}^{k_{nyq}} S(v, k_y) dk_y \quad (14)$$

The leakage of inappropriate wave energy into $S(v)$ is minimized by excluding energy at wavenumbers below an arbitrary minimum wavenumber, k_{min} (chosen as 0.125 m^{-1}). The upper limit of the integral is the Nyquist wavenumber, k_{nyq} , or $1/(2dx)$, where dx is sampling spacing.

The resulting velocity spectrum (Figure 2.5) has several typical features: a background energy pattern due to video noise and low frequency intensity patterns and a relatively large peak of energy representing the foam traces. Any energy associated with passing breaking waves crests, which is present mostly at wavenumbers below our cutoff k_{min} , has been eliminated and thus cannot significantly contaminate the $S(v)$ spectrum.

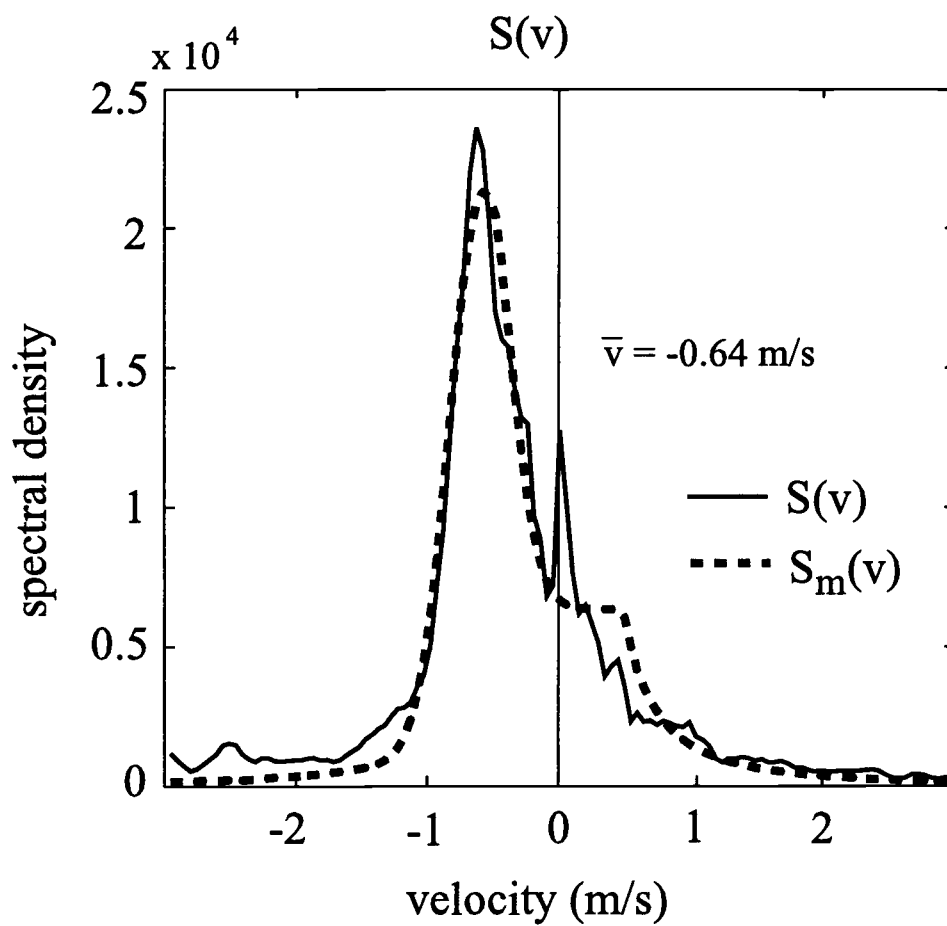


Figure 2.5 $S(v)$ spectrum derived from Figure 2.4. The model parameters and the final fit returned from the nonlinear fitting routine are also plotted.

2.2.4 $S(v)$ model

Because the $S(v)$ spectrum is complicated with energy from foam streaks, waves and background noise, it not trivial to determine a single surface velocity estimate. Methods to estimate a representative velocity based on bulk statistics of the velocity spectrum (e.g. the mean and median velocity) are biased by background energy leaked from waves and by noise. Just as problematic is utilizing the location of the maximum energy or largest peak as a velocity estimate, because spurious narrow peaks are not uncommon in the $S(v)$ spectrum.

Our method instead uses a nonlinear least-squares routine to fit a model of the velocity spectrum, $S_m(v)$, to the observed spectrum, $S(v)$. Since wave energy has largely been eliminated, our model includes two components, the signature of the background noise and that for oblique foam traces

$$S_m(v) = S_{foam}(v) + S_{noise}(v). \quad (15)$$

The foam trace variance, S_{foam} , is modeled as a Gaussian curve with amplitude A_{foam} , mean foam velocity \bar{v} and width σ_{foam}

$$S_{foam}(v) = A_{foam} \exp\left[-\frac{(v - \bar{v})^2}{\sigma_{foam}^2}\right]. \quad (16)$$

The noise background is derived by assuming an input white noise time series, with

energy distributed uniformly over $S(f, k_y)$. Transforming this white noise to the velocity spectrum yields

$$S_{noise}(v) = \begin{cases} A_{noise} \frac{f_{nyq}^2}{2v^2} & \text{for } |v| \leq \frac{f_{nyq}}{k_{nyq}} \\ A_{noise} \frac{k_{nyq}^2}{2} & \text{for } |v| > \frac{f_{nyq}}{k_{nyq}} \end{cases} \quad (17)$$

In the $S_{noise}(v)$ model A_{noise} is the noise amplitude factor, f_{nyq} and k_{nyq} are the sampling dependent Nyquist frequency and Nyquist wavenumber, respectively.

The model then depends on four parameters, A_{foam} , \bar{v} , σ_{foam} , and A_{noise} . An initial guess of the fitting parameters from (16) and (17) is generated using basic statistics of $S(v)$ and is passed, along with $S(v)$, to the nonlinear fitting routine. Parameters are initialized as follows. A_{foam} is taken as the peak energy value in $S(v)$, \bar{v} as the velocity value corresponding to the energy peak, σ_{foam} is guessed as 0.15 m/s and A_{noise} as the median value of $S(v)$. The fitting routine uses the Gauss-Newton method to iterate to a best-fit solution in the least-squares sense (Press *et al.*, 1992). In short, a merit function, $M(\beta)$, is established which measures the sum of the squared differences between the model, $S_m(v)$, and the data, $S(v)$

$$M(\beta) = \sum_{i=1}^N [S(v(i)) - S_m(v(i); \beta)]^2 \quad (18)$$

where β represents the parameter space for the model, $S_m(v)$. The gradient of the

merit function drives the parameter search as the nonlinear routine iterates to a solution along the steepest descent, towards a minimum of the merit function. A best-fit solution, $\hat{\beta}$, is determined when the merit function is near the minimum and stops changing, or changes less than a preset tolerance level.

2.2.5 Velocity estimate quality

The quality of the velocity estimate derived from the OCM algorithm is assessed by computing statistical measures of the “goodness-of-fit” of the model and the best-fit parameters to the data. Additionally, because this method is based on the presence of foam due to wave breaking, a method was devised to provide an objective filter to reject estimates based on non-breaking images.

The condition of the model fit to the data is described using a χ^2 statistic (Press *et al.*, 1992). This value is related to the merit function formulated in (18)

$$\chi^2 = \sum_{i=1}^N \left[\frac{S(v(i)) - S_m(v(i); \hat{\beta})}{\sigma(i)} \right]^2 \quad (19)$$

where $\sigma(i)$ is the standard deviation of the measurement error at each point i . In our case we do not know the measurement error *a priori*. We choose to assign $\sigma(i)$ as a constant for all i , 10% of the maximum value of $S(v)$, which allows for an objective measure of the statistical significance of the model fit regardless of total energy.

From the χ^2 statistic a significance level of overall fit can be found.

Confidence intervals on the parameters, $\hat{\beta}$, in the model are estimated using the gradient of the parameter space as determined from the nonlinear fitting routine. A quadratic form is fit to the gradient of the parameter space in the vicinity of the “best-fit” parameters to the data, which ideally lie at the global minimum of $M(\beta)$. The confidence intervals are estimated as the range of the parameters around $\hat{\beta}$, based on the quadratic form of the parameter space gradient, which give the best-fit parameters a 95% probability (likelihood) given the data (Press *et al.*, 1992).

We calculate a proxy for the degree of breaking and residual foam in the video record, I_{range} , based on the intensity histogram of a window of the timestack

$$I_{range} = I_{95} - I_{50} \quad (20)$$

where I_{95} and I_{50} , are the 95th and 50th percentile intensity values, respectively.

Figure 2.6 shows the intensity histogram of the section of timestack from Figure 2.2. As the value of I_{range} increases, so does the contrast and the degree of wave breaking and residual foam seen in the timestack. A threshold value for usable data is investigated in section 3.3.3.

2.2.6 Viewing angle velocity bias

We assume our pixel array comprising the longshore current pixel instrument to be at mean sea level over the length of time for the video collection. If this were true our estimate of the longshore current velocity would be unbiased.

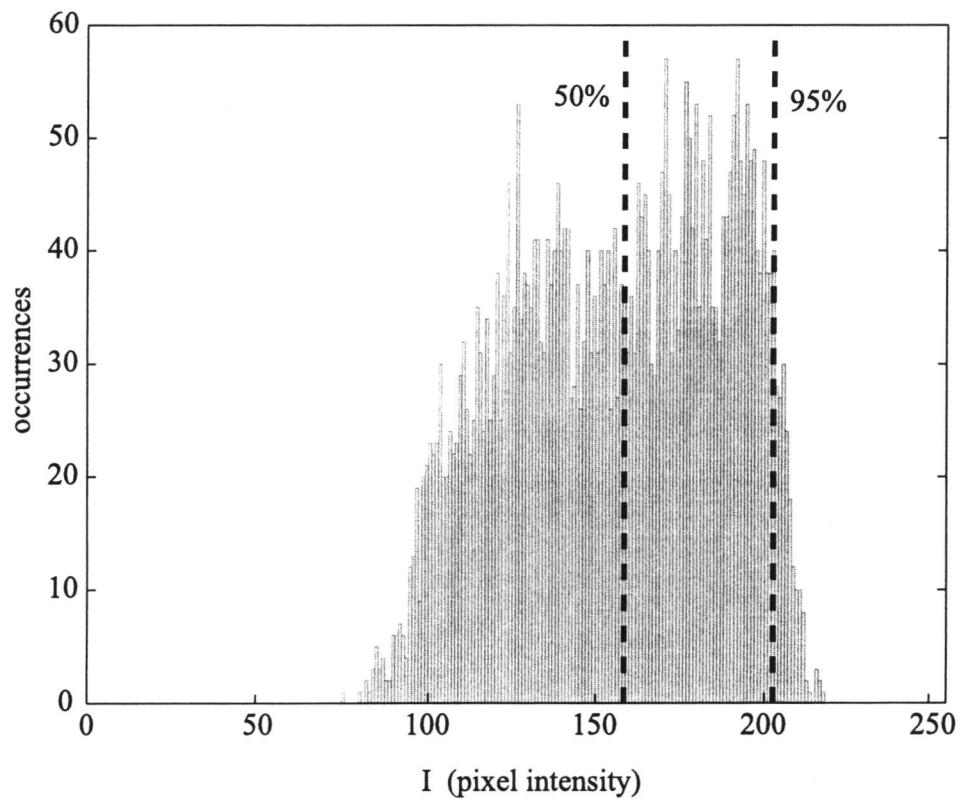


Figure 2.6 The sample histogram from a 32 s section of a timestack shows a broad range of image intensity. The dashed lines represent the 50th and 95th percentile intensities.

However, departures from mean sea level due to waves will cause a change in the apparent horizontal position of any pixel. Thus, a rate of change of sea surface elevation will appear as an apparent surface velocity. This apparent velocity will bias the estimated velocity of the longshore current in a linear way that would average to zero if foam variance were distributed uniformly over the wave.

However since this is not true, because we do not track drifting foam as the breaking wave crest passes, a mean bias is introduced. In this section we will construct a simple model of the velocity bias in order to correct the Optical Current Meter estimates.

Our model follows the standard pinhole camera assumption that light rays travel in straight lines from the real world objects we observe, through a focal point, to the image plane (Wolf and Dewitt, 2000). The camera's pinhole is located at (x_c, y_c, z_c) and the point being observed in the real world is at (x_p, y_p, z_p) . The parametric equations for the line of sight from the camera to the point of observation in space are:

$$x = x_c + s(x_p - x_c) \quad (21a)$$

$$y = y_c + s(y_p - y_c) \quad (21b)$$

$$z = z_c + s(z_p - z_c) \quad (21c)$$

in terms of the dummy variable s .

For simplicity, we model the variable sea surface as a regular saw tooth wave, incident at angle α , such that there is a discontinuous finite jump where the trough of the previous wave immediately precedes the next crest. Therefore, the shape of the free water surface for one wave period is:

$$z = \frac{-(x - Ct)\cos(\alpha) - (y - Ct)\sin(\alpha)}{\tan(\pi/2 - \beta_s)} \quad \text{for } 0 \leq t < T \quad (22)$$

where β_s is the maximum sea surface angle, C is the wave celerity and T is the wave period.

We solve for the change of the alongshore position, v_{apparent} , of the intersection of the camera's line of sight with the moving wave surface with respect to time by using (21a), (21b), (21c) and (22) to solve for y and taking its derivative with respect to time.

$$v_{\text{apparent}} = \frac{C(y_p - y_c)}{(x_p - x_c)\cos(\alpha) + (y_p - y_c)\sin(\alpha) - (z_p + z_c)\tan(\pi/2 - \beta_s)} \quad (23)$$

The solution describes the alongshore directed apparent velocity of the surface that we are viewing due to the passing wave. Thus, the correction is applied to the mean velocity estimates as

$$\bar{v}_s = \bar{v}_{OCM} - v_{\text{apparent}} \quad (24)$$

The pinhole of the camera is assumed to be stationary over time, and the position of

the point in space the camera views is taken as the center location of the real world coordinates of the longshore pixel array. Discussion of the magnitudes and the nature of this correction for the test cases occurs in chapter 4.

2.2.7 Generating a time series

A time series of longshore current velocity, v , is estimated by applying the OCM algorithm in a step-wise fashion through the video, so that the window of analysis overlaps the previous window by some amount of time. The time length of the analysis window, T_l , and the time length of the step, T_s , are both unrestricted constants, though because the OCM algorithm estimates the mean foam velocity for the selected section of video record, the choice of T_l and T_s depends upon the frequency of the signal of interest that we wish to resolve. In the next section, we test the performance of the OCM algorithm for different lengths of T_l by applying the OCM to synthetic data sets for which we have absolute knowledge of the breaking, foam patterns and longshore current properties.

2.3 Synthetic Data Tests

2.3.1 Synthetic timestacks

Idealized timestacks were constructed to include the alongshore drift of sea foam in the presence of a mean longshore current, the contribution of the alongshore component of surface wave orbital velocity, and the visual signature of

the shoreward-propagating breaking wave front.

The longshore velocity field over time t is modeled

$$v(t) = \bar{v} + v_o \cos\left(\frac{2\pi t}{T}\right) \quad (25)$$

where v_o is the alongshore wave orbital amplitude and T is wave period. Surface foam is assumed to drift with the same velocity as the longshore current with no time lag.

The visual signal of foam streaks is modeled as the sum of sinusoidal variations in the image intensity in the alongshore direction. Since a range of characteristic sea foam wavelengths exists in a natural surf zone environment, we assume a uniform distribution of energy over a set of wavelengths, from 2 to 15 meters. The pattern of foam patches is regenerated with random phases which are reset with the passing of each breaking wave crest. The passing wave front is depicted as a bright horizontal band of constant intensity appearing at every integer multiple of the wave period in the timestack, simulating a monochromatic wave field. Finally random noise was added to the stack. Two examples of synthetic stacks are shown in Figure 2.7.

2.3.2 Mean current estimation

Synthetic stacks with a constant wave period of 8 s were created using a

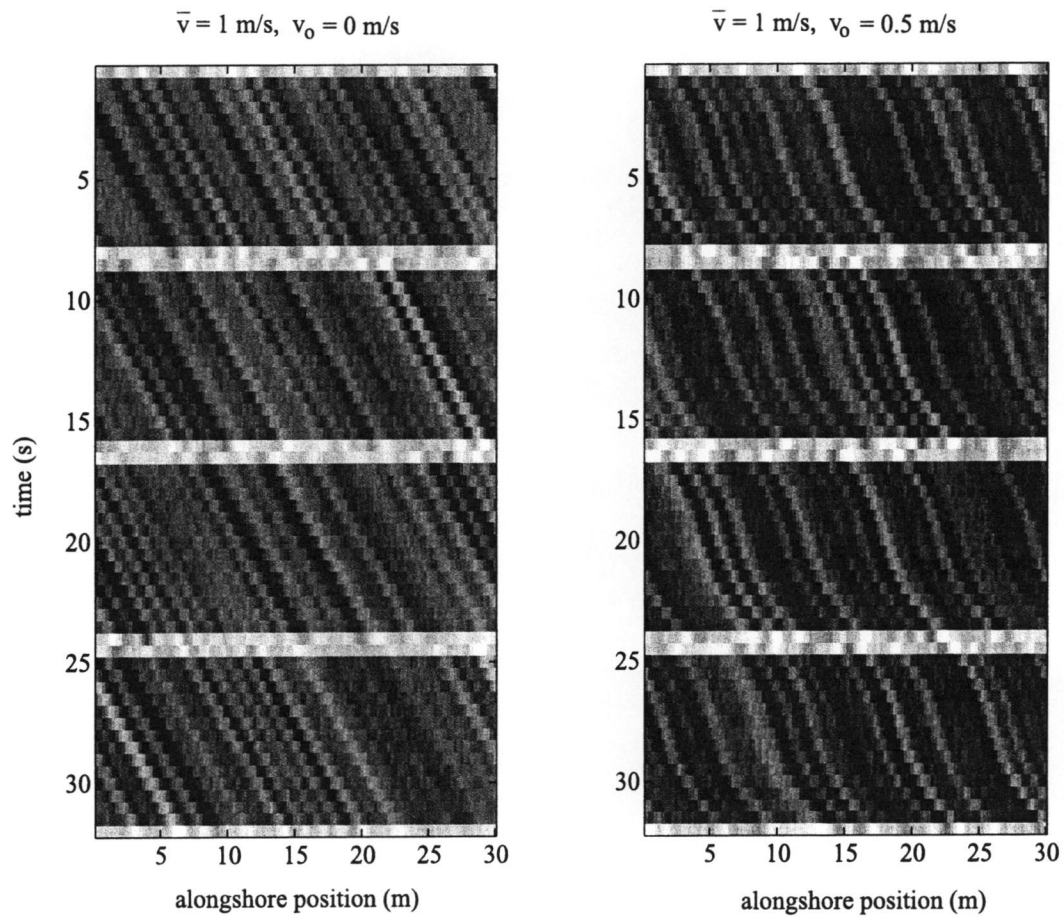


Figure 2.7 Synthetic stack examples. The left panel is an example of a synthetic timestack with advected foam (oblique traces) moving at a constant 1 m/s and breaking waves (horizontal bright lines). The right panel has foam advecting at an average of 1 m/s with an added sinusoidal velocity variation with amplitude 0.5 m/s.

range of mean velocities from 0 to 1.5 m/s, the typical range observed in the field. The alongshore amplitude of orbital velocity, v_o , was allowed to vary from 0 to 0.5 m/s, to simulate varying degrees of contamination by obliquely incident waves. The maximum value, 0.5 m/s, corresponds to a shallow water wave with a height of 1 m approaching the shoreline at 27° from normal or a 2 m wave approaching at 13° from normal incidence.

The OCM algorithm is applied to each synthetic stack using different analysis window lengths, T_l . The choices for T_l are made to include an integral number of wave periods from 8 to 64 s in increments of 8 s. This will eliminate bias of the estimation due to sampling less than a full wave period. Each synthetic stack created is a single realization of an infinite set of possibilities, therefore each velocity estimation by the OCM algorithm is a single estimate of the true model mean current, \bar{v} . For each combination of T_l , \bar{v} and v_o ten realizations of the synthetic timestacks were created, the mean current was estimated, and the results averaged over the ten realizations. A second test was conducted with synthetic timestacks of varying wave period (8, 10, 12, 14 and 16 s), and constant T_l , to determine if non-integer wave period sampling has an effect on the velocity estimation. Again, ten timestacks for each combination of T , \bar{v} and v_o were created, the mean current was estimated and the results were averaged.

2.3.3 Results

The results of the first synthetic stack test are plotted in Figure 2.8. In general, the OCM performed as expected; the optically estimated mean velocities are in very good agreement with the actual mean longshore velocities over a range of mean velocities and orbital velocity contamination. It is apparent that as the length of the window of analysis (T_l) is increased, the accuracy of the OCM increases for all the mean velocities considered. Figure 2.9 shows that the total root-mean-square error decreases with increasing T_l , although there is little change for T_l larger than 32 s. Figure 2.8 also shows that at lower true mean velocities the results from the OCM proved to be more scattered, particularly for T_l equal to 8 and 16 s.

The final choice of T_l balances the RMS error reduction gained by using longer T_l , with the decreased smoothing of a velocity time series gained by using shorter T_l . Additionally, we are concerned with the scatter in the estimates at low mean velocities and shorter T_l . For this reason, subsequent analyses are based on T_l equal to 32 s, as little error reduction was gained by doubling the window length to 64 s, but the scatter at low velocities is reduced as compared to a window length of 16 s.

The results of the synthetic test with $T_l = 32$ s, but varying the synthesized wave period, also showed that the OCM performed well (Figure 2.10) even though

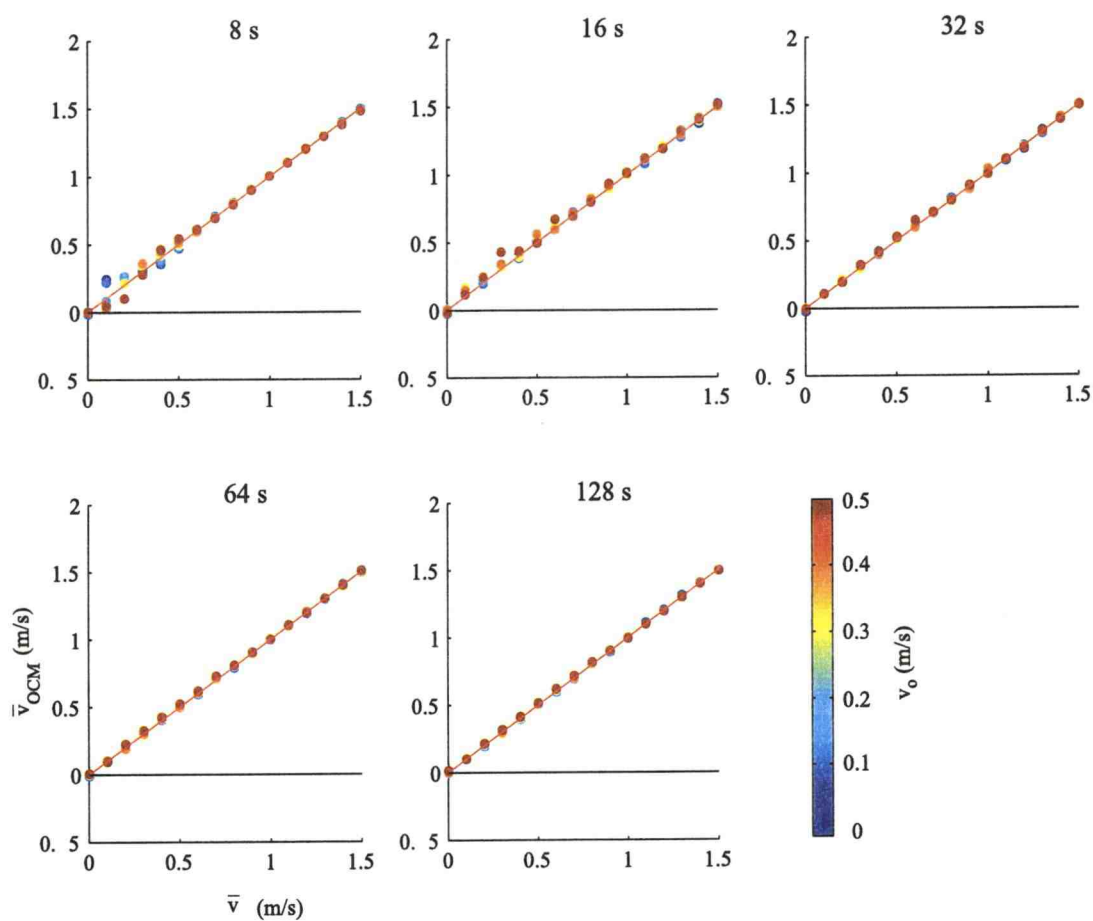


Figure 2.8 The results from the synthetic stack test of the OCM for various window lengths, T_l . The OCM estimated mean velocity is plotted versus the actual mean velocity. The length of the sampling window in seconds is denoted above each plot. The colors of the plot indicate the strength of the maximum variation in the wave orbital velocity from zero (blue) to 0.5 m/s (red).

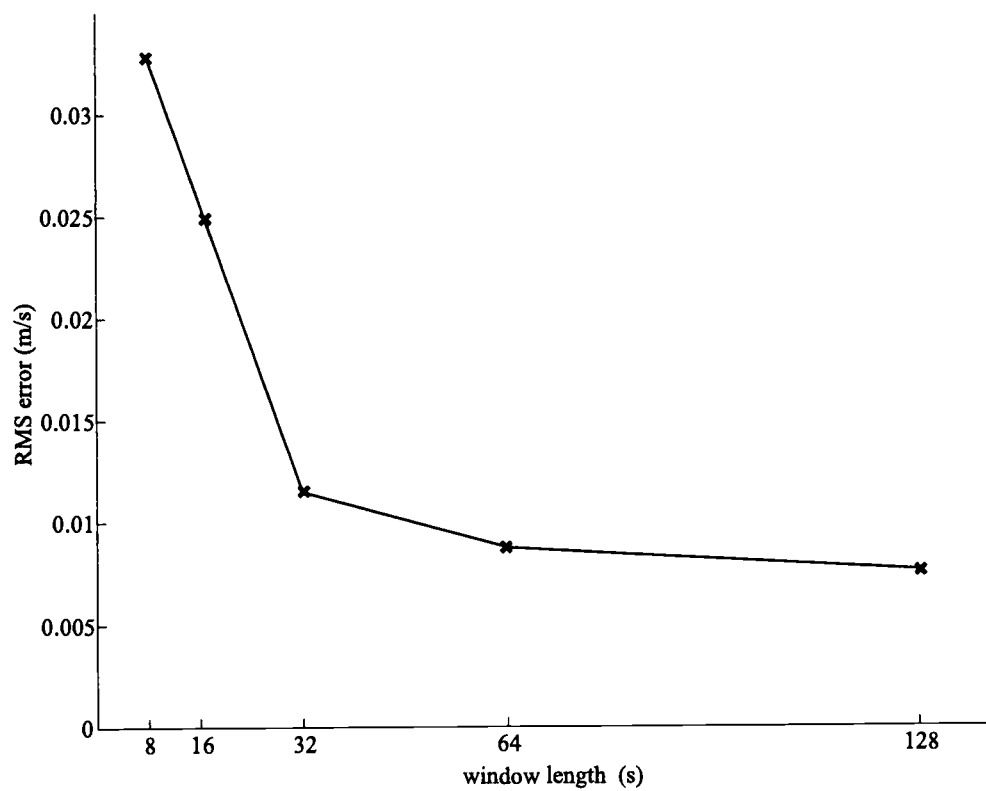


Figure 2.9 Total root-mean-square error for each window length, T_l , over all mean velocities and maximum orbital velocities.

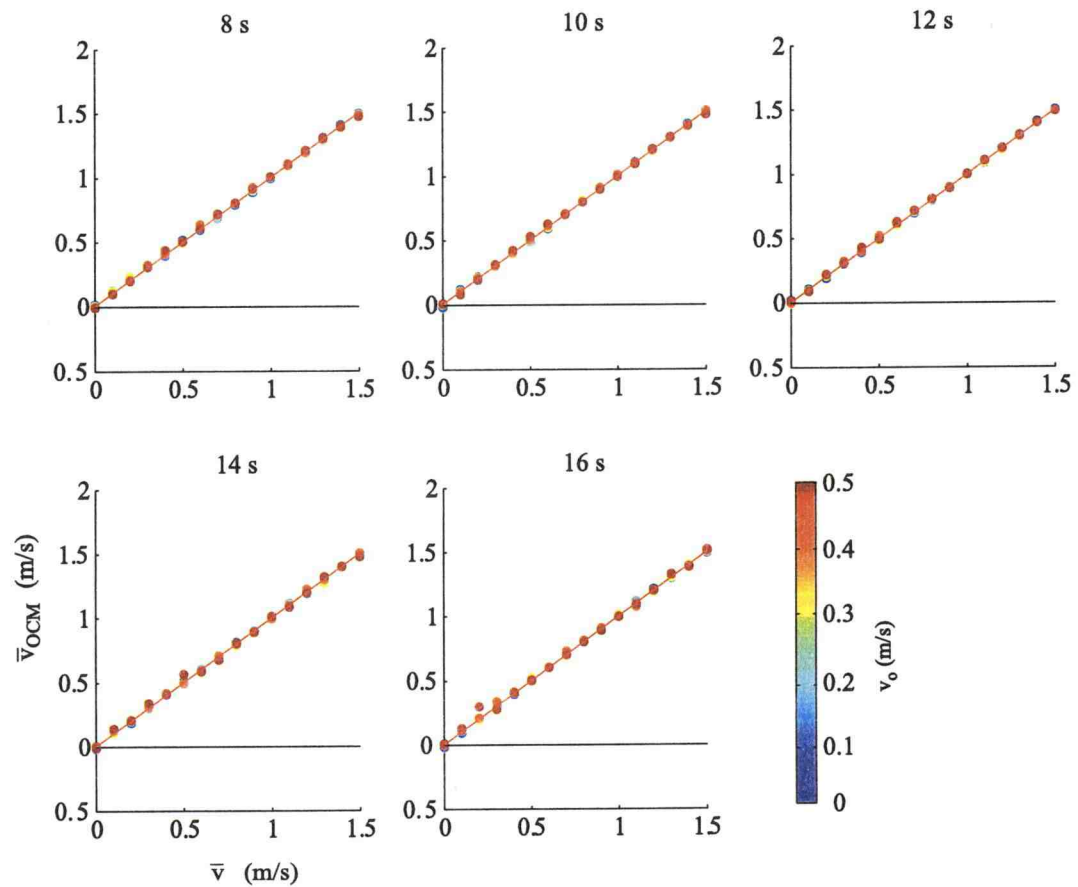


Figure 2.10 The results from the synthetic stack test of the OCM for various wave periods and constant window length, $T_l = 32$ s. The actual mean velocity is plotted versus the OCM estimated mean velocity. The wave period is denoted above each plot.

non-integer wave periods were used (10, 12 and 14 s). The RMS error (Figure 2.11) for this test is less than 0.02 m/s over the range of simulated conditions. Presumably, the extended length of the sample (32 s), reduces any bias that may be introduced by sampling less than a non-integer multiple of the wave period.

2.3.4 *Velocity bias due to aliasing*

For our synthetic tests we modeled foam patches that were greater than 2 meters in wavelength, though when a strong mean longshore current and short wavelength (less than 2 m) foam exists our OCM may introduce an apparent velocity bias due to aliasing. Since the apparent frequency of foam drift is given by $\nu \cdot k_y$, for high values of ν and k_y the apparent frequency may lie outside of the Nyquist frequencies, $\pm 1/(2dt)$, where dt is the sampling spacing in time. Energy outside of this range will be mapped into other inappropriate frequencies, a phenomenon known as aliasing.

In the final calculation of the velocity spectrum, $S(\nu)$, any aliased energy is spread out over a velocity range often far from the original velocity. In the case where there is a velocity band, as when the velocity time series has a wave orbital component, at any particular wavenumber band there is energy present at a range of frequencies. If the velocity or wavenumber band width is large enough a portion of the energy corresponding to higher magnitude velocities in that wavenumber band may be aliased into other frequencies. The aliased portion of the energy is spread

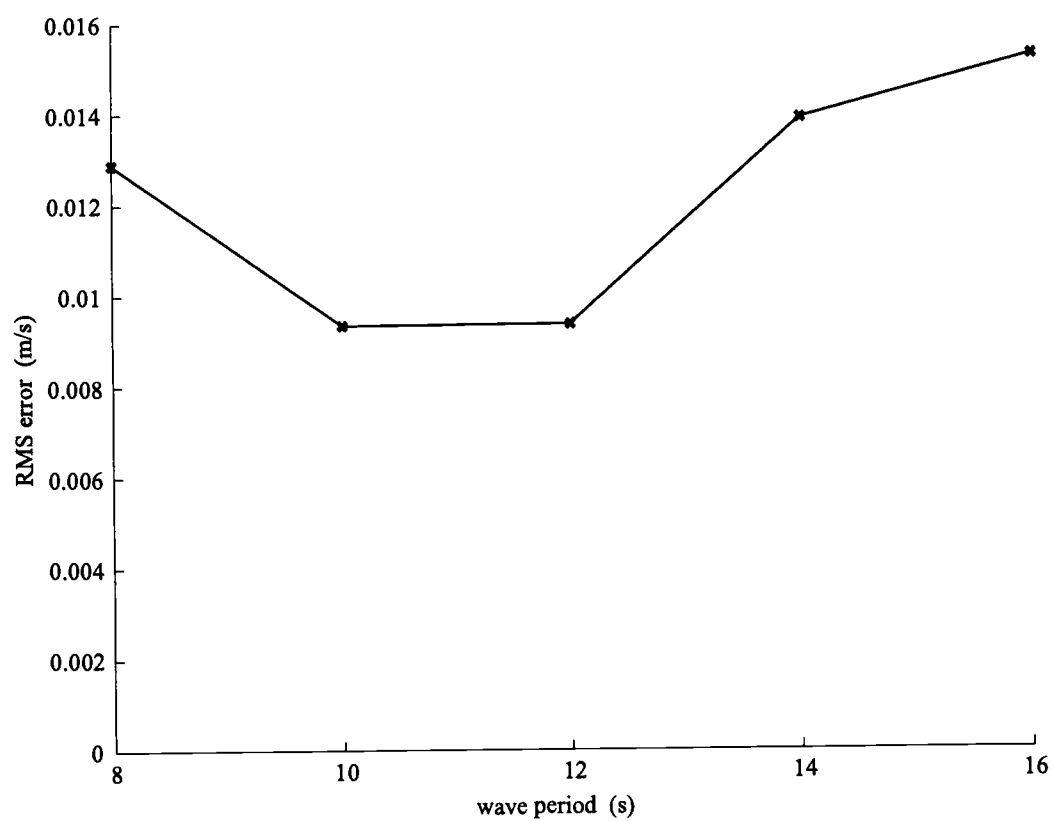


Figure 2.11 Total root-mean-square error for each wave period for all mean velocities and orbital velocity amplitudes.

out over other velocities when the velocity spectrum is calculated, while the energy in the lower portion of the velocity band is not, leaving a bias toward lower velocities. The problem could be rectified by simply increasing the sampling rate above 2 Hz. For example, given 4 Hz sampling the Nyquist frequency is 2 Hz, and for 1 m wavelength foam patches the maximum resolvable velocity is 2 m/s, but since we believe that the foam wavelengths resolved by video imaging are mostly longer than 1 m, a faster sampling rate would provide little, if any, benefit.

Chapter 3: Field Test

3.1 Introduction

To demonstrate the viability of the optical current meter to collect field measurements, a comparison of OCM estimates of the mean longshore current with mean longshore currents measured by an *in situ* current meter was carried out. While our optically based current meter measures the surface expression of the longshore current, conventional current meters (e.g. electromagnetic, acoustic and impeller types) necessarily sample the interior currents, so our comparisons between the two are not direct. However, previous studies (e.g. Garcez Faria *et al.*, 1998) have shown that there is little vertical shear in longshore currents, except near the seafloor, so the comparison should be useful. This chapter details the approach and results of the field test of our optical current meter.

The field test was conducted on a sandy beach on the Outer Banks of North Carolina at the Field Research Facility (FRF) in Duck, a research station operated by the U.S. Army Corps of Engineers (Birkemeier *et al.*, 1985). The Outer Banks is a series of barrier islands extending along the North and South Carolina coasts. The mean beach slope across the steeper foreshore is 0.08 and the more gently sloping offshore portion is about 0.01 (Plant *et al.*, 1999). The average significant wave height is 0.9 m (Birkemeier, 1985). This beach is classified as intermediate in

the morphodynamic classification of Wright and Short (1983), with an Iribarren number of 0.35. The submerged portion of the beach in the vicinity of the FRF usually has one or two bars present throughout the year. Bar movement typically shows a seasonal pattern, with the bars migrating offshore in the winter and returning in the summer, in addition to an interannual trend of offshore migration (Plant *et al.*, 1999). The wave (peak wave period, significant wave height, wave angle) and wind speed conditions during the field experiment are summarized in Table 1.

Table 1 Wave and wind conditions during SandyDuck

	<i>mean</i>	<i>maximum</i>	<i>minimum</i>
H_0 (m)	0.98	3.44	0.31
T_p (s)	9.3	15.6	3.7
α ($^\circ$)*	3.7	51.6	-34.6
W (m/s)	5.5	18.4	0.03

* positive angles indicated waves coming from the north

3.2 In Situ Data

The comparison data was obtained during the 1997 SandyDuck field experiment, a multi-investigator collaboration targeting the investigation of sediment transport in the surf zone and the likely forcing mechanisms, waves and currents (Birkemeier *et al.*, 1996). A team led by Steve Elgar and Robert Guza collected measurements of water flows in the surf zone using an array of bi-

directional electromagnetic current meters (Elgar *et al.*, 2001). Pressure sensors collocated with each current meter were used to collect water surface elevation measurements, later used to estimate the local wave heights. The horizontal and vertical coordinates and the elevation of the *in situ* instruments above the seafloor were collected and recorded as auxiliary data.

The array of *in situ* current meters consisted of 33 individual instruments, although in this field test the *in situ* longshore current data from only one instrument was used (Figure 3.1). The *in situ* data for this test spanned the time from October 1, 1997 to November 11, 1997. Measurements of longshore velocity, cross-shore velocity and surface elevation were recorded at 2 Hz in three hour continuous blocks with slight gaps between blocks. Longer gaps in the records were due to the periodic emergence of the instruments at low tide. Data runs for which the significant wave height was greater than the mean water depth, both based on the collocated pressure sensor measurements, were removed from consideration. Additionally, instruments occasionally required removal for repairs producing other data gaps.

Prior to comparisons between *in situ* longshore current time series estimates, v_i and optical estimates of the time series of surface longshore current, v_s , pretreatment was necessary. The v_i time series was smoothed with a running boxcar window with a window length equal to T_l (the time length of window of

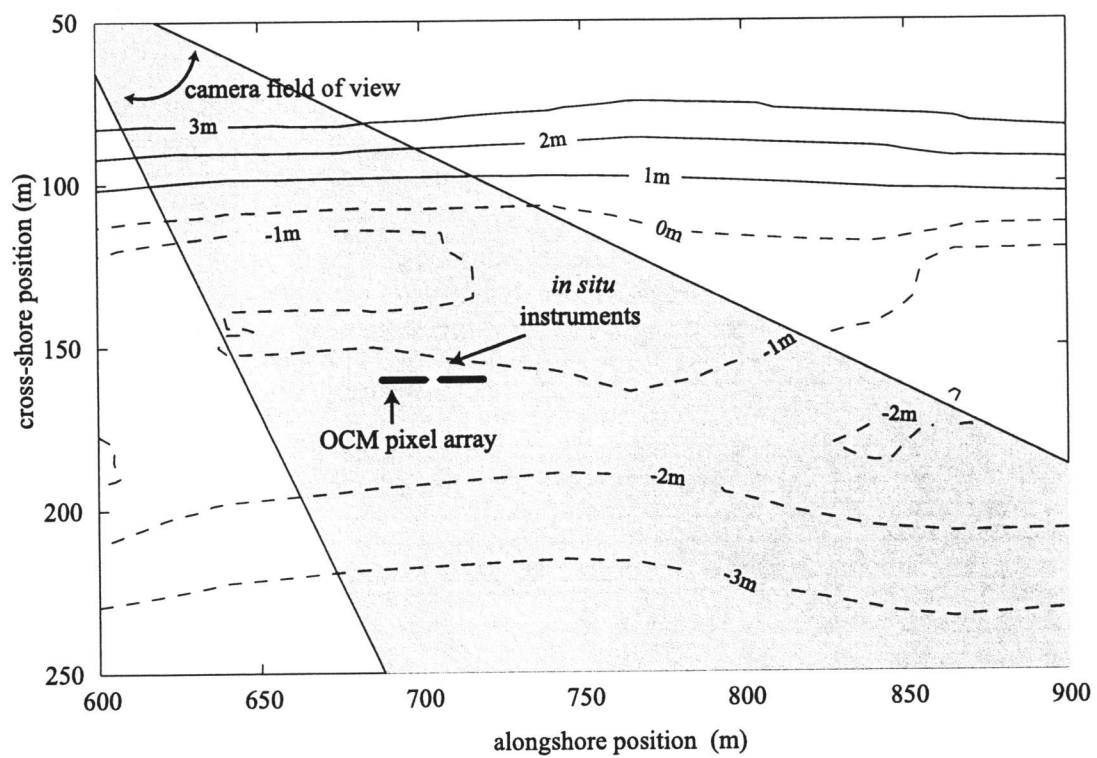


Figure 3.1 Plan view of the collocated current meters and pressure sensors, bathymetry and OCM pixel array.

analysis in the OCM algorithm) and sub-sampled with a new sampling spacing of T_s to match the sample spacing and smoothing characteristics of the v_s time series, discussed in the next section. Sub-sections of the smoothed and sub-sampled v_i time series corresponding to the individual 17 minute records were then extracted for the ground truth comparison.

Wind and wave information used in this analysis is gathered routinely at the FRF. Mean wind speed and direction measurements were collected from a meteorological station at the end of the FRF pier at a height of 19.36 m. These measurements were converted to estimates of alongshore wind stress, using equation (9), with the drag coefficient as formulated by Large and Pond (1981).

Wave directional and frequency spectra were derived from 3 hour records of surface elevation time series recorded from a 15 element array of pressure sensors located ~900 m offshore of the FRF (Long and Oltman-Shay, 1991). From these direction-frequency spectra a measure of the resultant wave direction α is estimated. Information used to calculate the other wave based parameters are taken from the *in situ* pressure sensor records. The standard deviation of the water surface elevation time series, σ_η , was calculated and used to estimate the mean wave height (Dean and Dalrymple, 1984), using

$$\bar{H} = 2.5035 \sigma_\eta. \quad (26)$$

The wave celerity is calculated using shallow water linear wave theory wave

$$C = \sqrt{gh} \quad (27)$$

where h is the local water depth. The wave steepness angle, β_s , was calculated using the mean wave height H_0 and the wavelength, L , where

$$L = CT_p \quad (28)$$

and T_p is the peak wave period estimated from the frequency spectrum of the *in situ* pressure sensor records (Jenkins and Watts, 1968).

3.3 Video Data

3.3.1 Collection

During the 1997 SandyDuck field experiment video data were collected from an OCM pixel array centered on the horizontal location of the *in situ* instrument cluster '11' (Figure 3.1 and pictured in Figure 3.2). The vertical coordinate of the pixel array was determined from the predicted tide level at the time the video data were recorded. The details of the optical array and how the pixel locations of real world coordinates were determined as described in section 2.2.3. Video timestacks were collected during the daylight hours, once each hour for 1024 s (17 minutes) at 2 Hz from October 1 to November 11.

Prior to processing, timestacks with poor video quality were identified and



Figure 3.2 A camera view of the longshore pixel array (oblique line) used for the field test. The horizontal location of the collocated *in situ* current meter is marked with an 'x'.

eliminated. The most prevalent problems were sun glare and low ambient light levels at dusk. Removing video data runs between the hours of 1700 and 0900 EST was an effective solution. A more uncommon problem was rain on the camera lens. This could not be detected automatically so a manual search was required. Three days, October 15, 19 and 26, exhibited rain contamination; accordingly, all of the data from those days were removed.

3.3.2 OCM processing

For each hourly video record a time series of surface longshore current, v_s , was estimated using the OCM algorithm. The time length of the window of analysis, T_l , was set to 32 s and the time step, T_s , was 16 s (for a 50% overlap). This produced a 63 point time series of surface longshore current for each individual 17 minute video record (e.g. Figure 3.3).

The alongshore pixel array was designed to be centered on the horizontal real world location of the *in situ* current meter, which is mounted on a dark metal frame. Unfortunately, at low tide the frame was exposed and was sampled as part of the video data. This left a long dark trace throughout the timestack, because the frame does not move, (e.g. Figure 3.4). When a stack contaminated in this way was analyzed with the OCM algorithm, the strong signal of the dark unmoving frame produced a velocity estimate that was biased low, and often the velocity signal of the frame was large enough to produce a zero velocity estimate even when foam

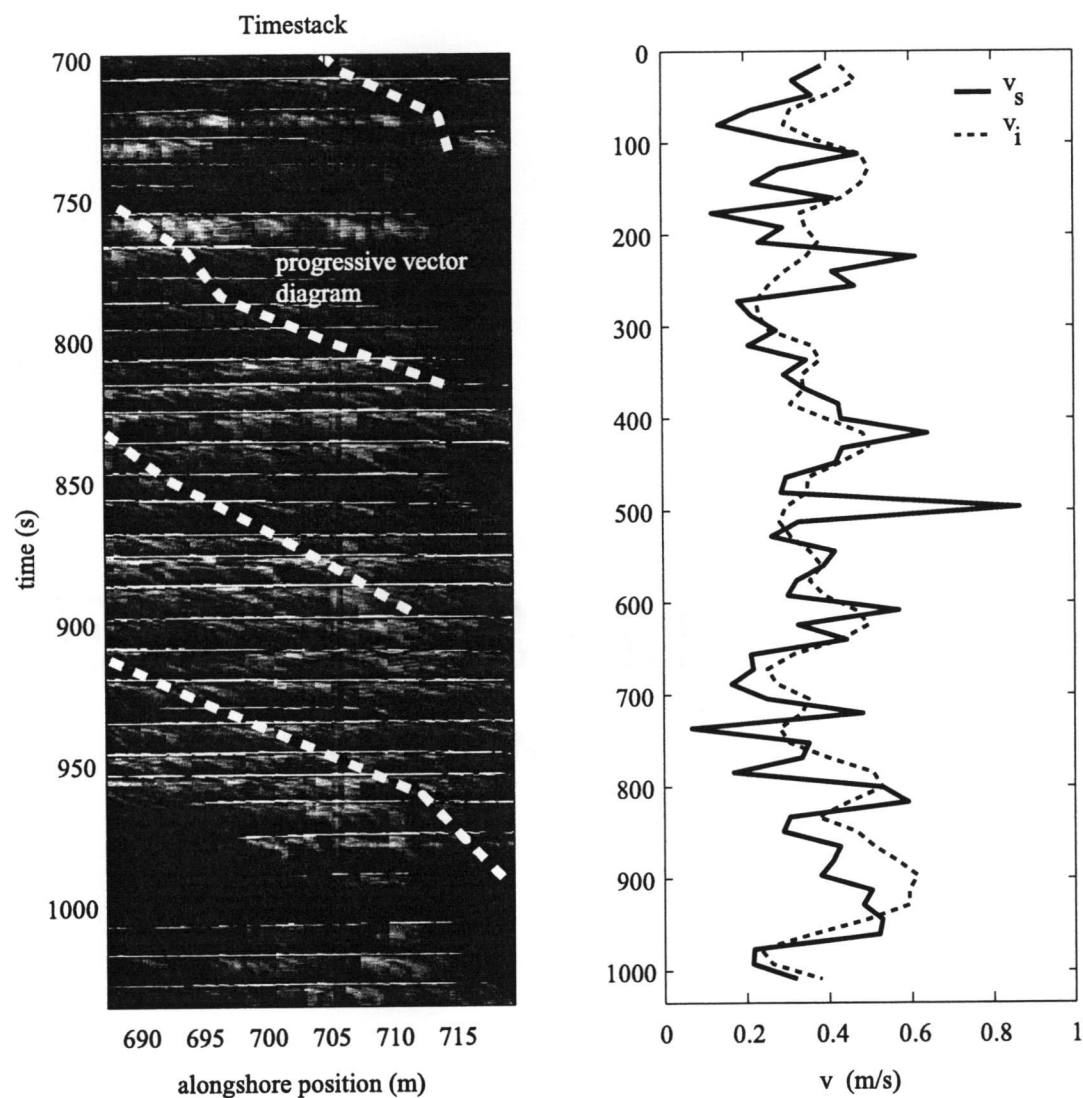


Figure 3.3 Sample timestack (left panel) with superimposed progressive vector diagram (PVD) and longshore current time series (right panel). The PVD is the stepwise integrated surface velocity time series v_s . Note that the timestack and PVD are only a portion of the full 1024 s timestack. The data were taken on Nov. 4, 2034 GMT.

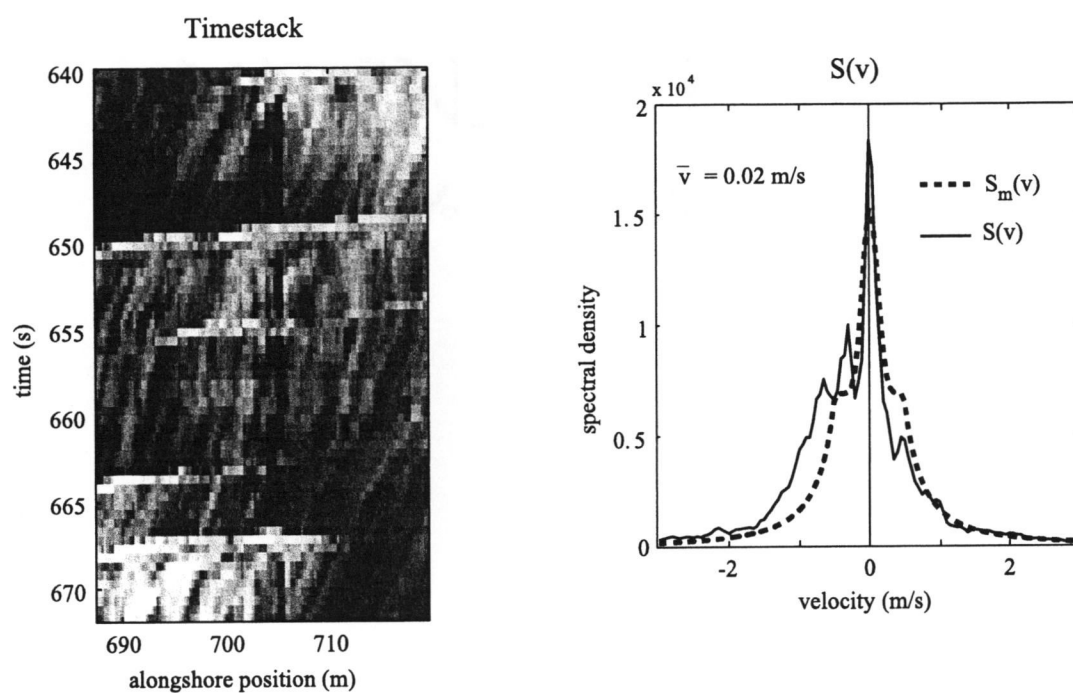


Figure 3.4 A section of a timestack, on the left, taken on Oct. 2 at 1534 GMT. It shows the contamination of the in situ sensor frame as dark vertical traces. The resulting velocity spectrum and velocity model fit is shown in the right panel.

streak traces dictated otherwise (Figure 3.4).

This problem was circumvented by splitting every timestack into two equal sections in the alongshore (spatial) direction, one on either side of the contaminated middle section. The frame was assumed to be unmoving for the duration of the experiment, so the contaminated section to be removed from each stack was conservatively fixed as the area between 701 and 707 m in the alongshore coordinate (see Figure 3.1). $S(f, k_y)$ spectra were computed from each sub-timestack independently and averaged together. An example of a divided stack and the resulting $S(v)$ spectrum is shown in Figure 3.5.

3.3.3 Wave breaking filter

A threshold value for I_{range} (described previously) was chosen based on the distribution of absolute deviations of the optically calculated surface longshore velocities from the *in situ* longshore velocities as a function of I_{range} (Figure 3.6). The threshold of $I_{range} > 40$ was used for the remainder of the tests and is recommended for future analyses.

3.4 Ground Truth Test Results

For the following ground truth tests, OCM data points were deemed acceptable if they satisfied three criteria: (1) greater than a 90% significance of fit from the model skill (§ 2.2.4); (2) a 95% confidence range of less than 0.2 m/s (\pm

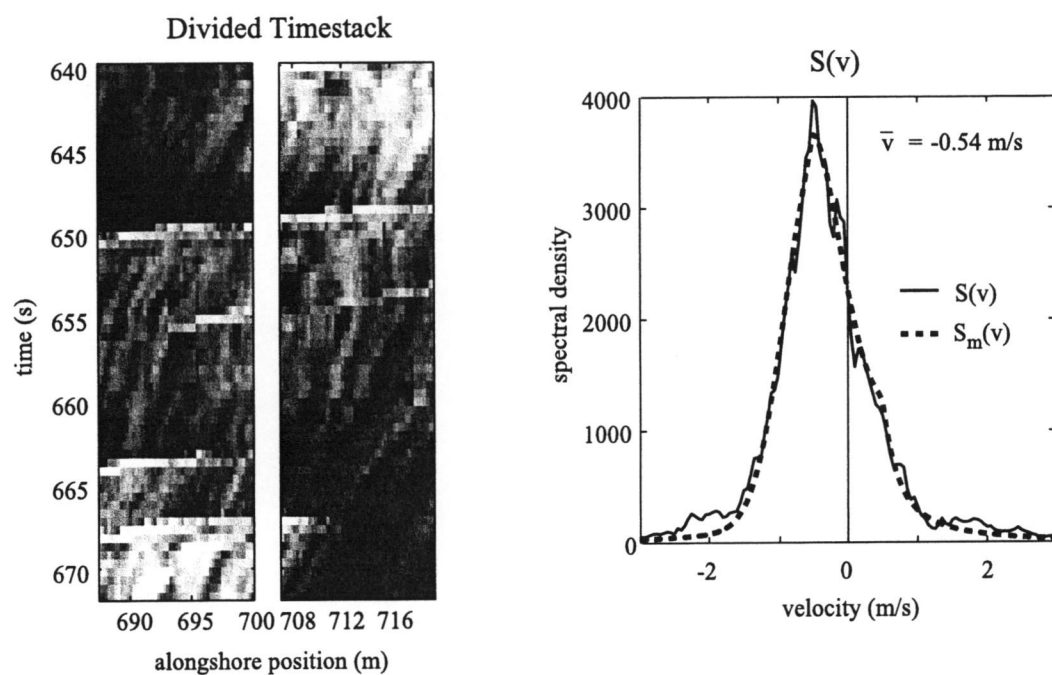


Figure 3.5 The same stack from Figure 3.3, with the contaminated middle section removed (left panel). The resulting $S(v)$ derived from the average of the $S(f, k_y)$ spectrum from each separate sub-timestack is on the right.

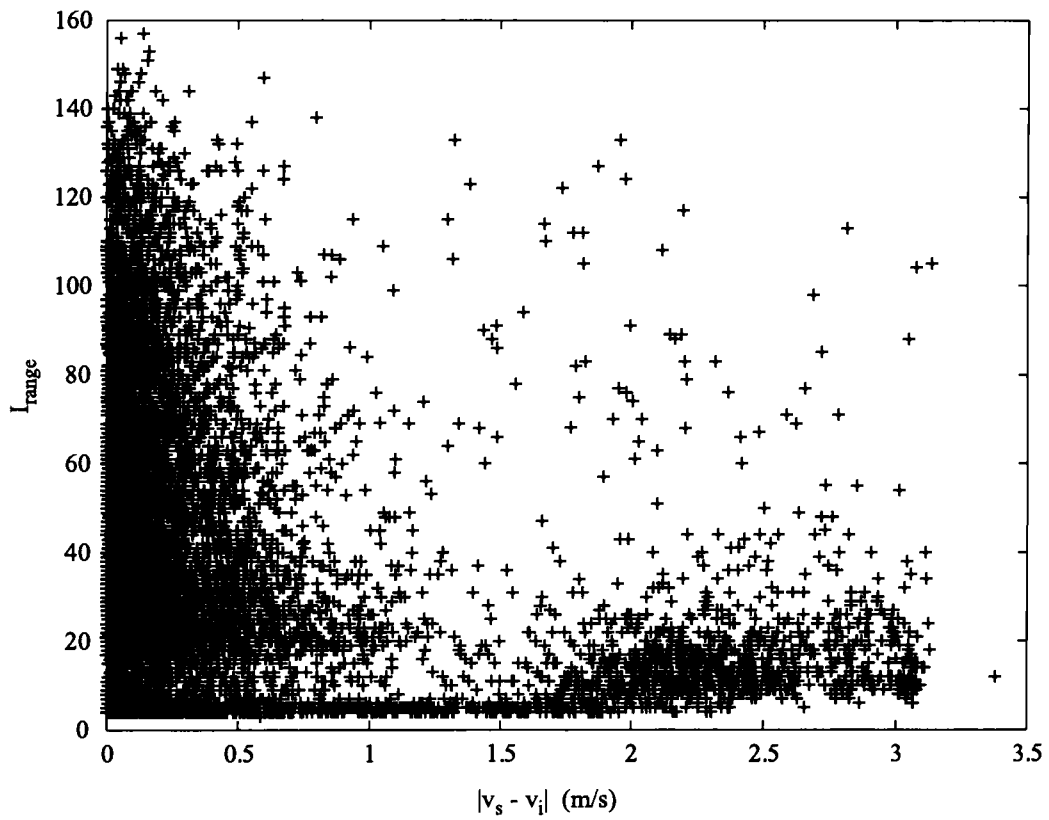


Figure 3.6 I_{range} variable compared with the absolute deviation of surface currents from interior longshore currents. I_{range} is the intensity span from the 95% to the median intensity value.

0.1 m/s) (§ 2.2.5); and (3) $I_{range} > 40$ (§ 3.3.3). Fifteen example time series of surface longshore currents, which retain at least 75% of the original velocity estimates after the quality control procedures, are plotted in Figure 3.7 along with the corresponding *in situ* records. A cross-correlation calculated between each pair of records (also in Figure 3.7) shows that all but three of the time series pairs are significantly correlated (at a 95% significance level), with the surface OCM time series capturing most of the low frequency variations seen in the *in situ* time series.

The mean velocities from the *in situ* and OCM estimates were also compared. A mean velocity was calculated if at least ten (10) out of 63 estimates for each time series passed these criteria. Of the 307 stacks collected and acceptable mean velocity was calculated for 109 of them. Figure 3.8 shows a time series comparison of mean longshore current estimates from the Optical Current Meter with ground truth data returned from the *in situ* longshore current meter. The mean OCM longshore surface currents, \bar{v}_s , and *in situ* longshore currents, \bar{v}_i , correspond closely in magnitude and sign for the majority of the record.

A more direct comparison between the two estimates is shown in Figure 3.9, where \bar{v}_s plotted versus \bar{v}_i . Were the surface and interior velocity estimates in perfect agreement the data would lie along the line of unity slope. The overall agreement between the two is very good with little scatter and with a significant linear least-squares fit having slope 1.0 ± 0.1 (95% error) and intercept 0.01 m/s.

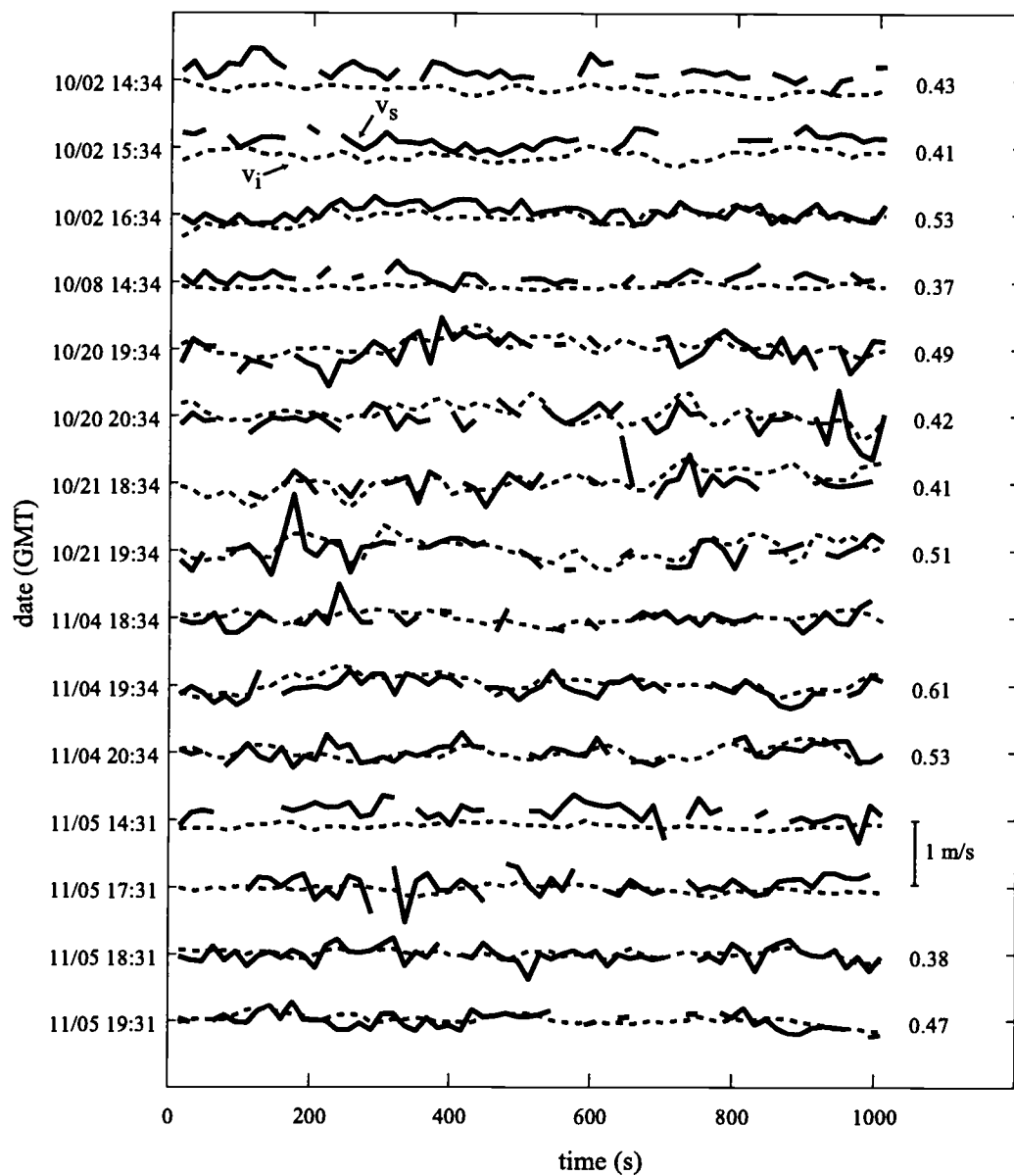


Figure 3.7 Fifteen sample surface (solid lines) and interior (dashed lines) longshore current time series. Only surface current data passing the criteria described in the text are plotted. The cross-correlation value computed for each time series pair is listed to the right, non-statistically significant correlation values are omitted.

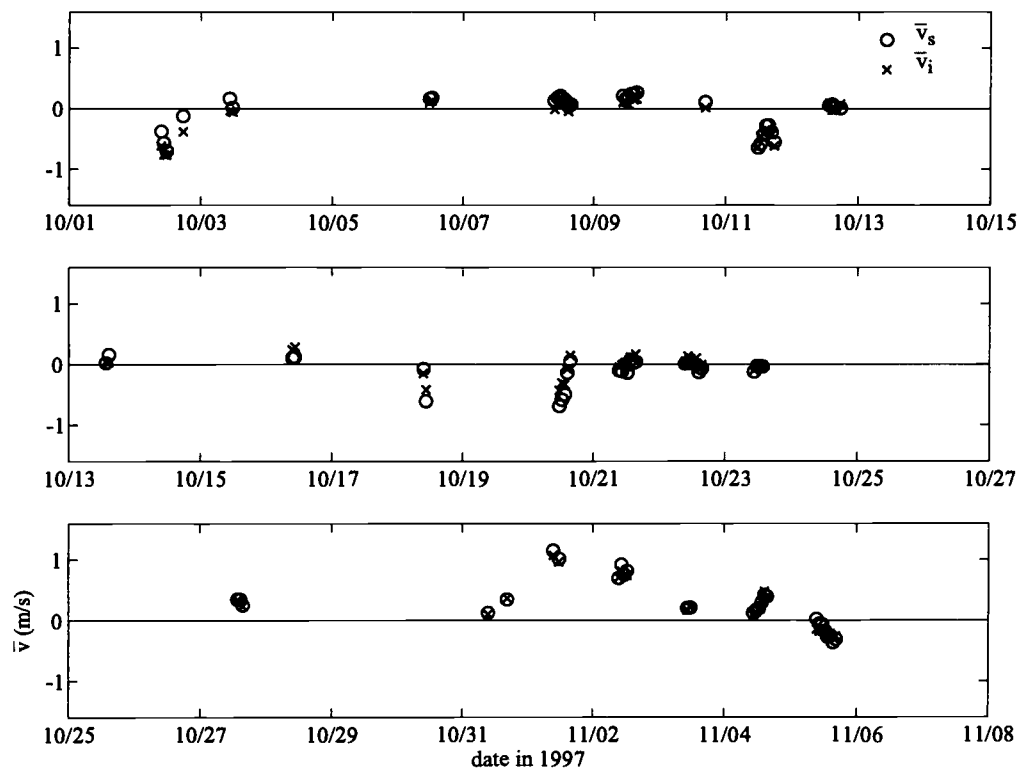


Figure 3.8 Optically measured mean surface currents ('o') and *in situ* currents ('x') for October and the first week of November, 1997, at Duck NC.

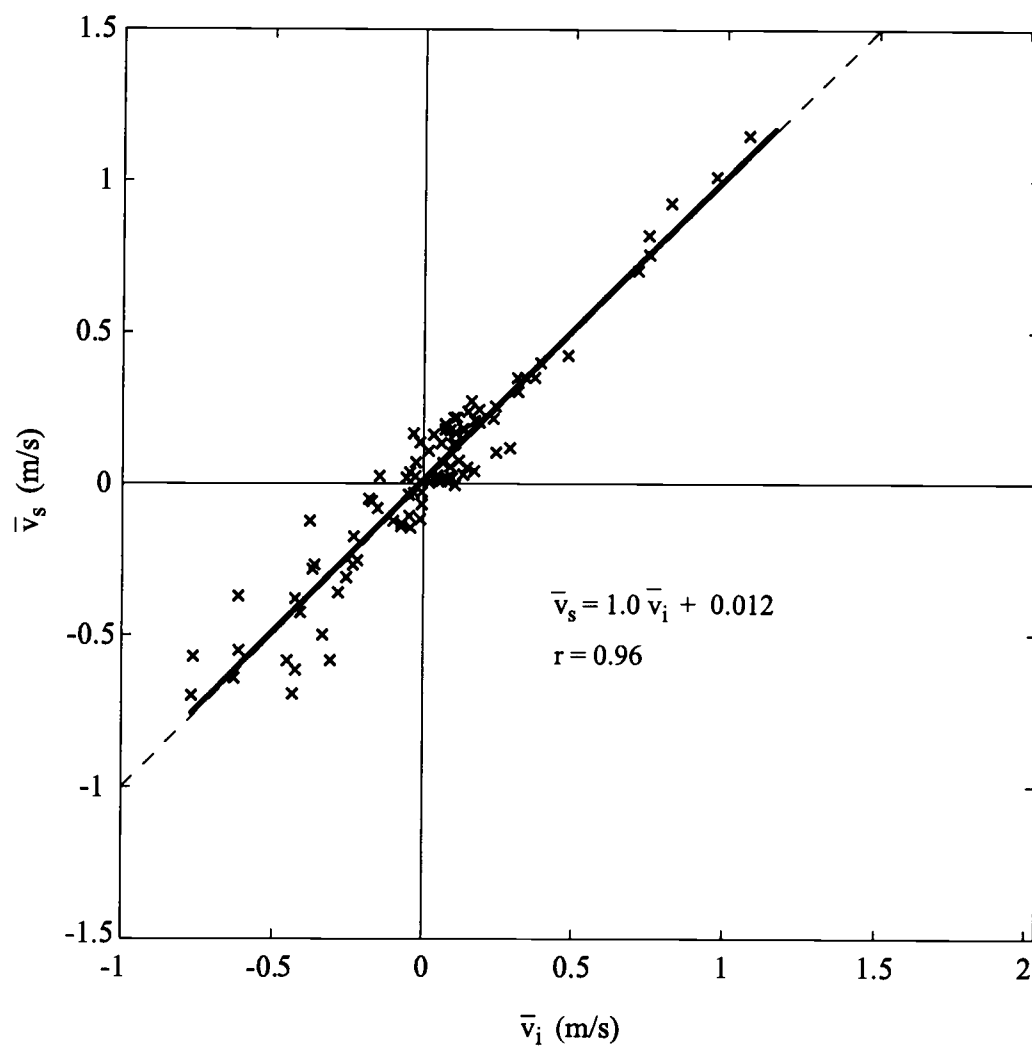


Figure 3.9 *In situ* longshore current means, \bar{v}_i , versus surface longshore current means, \bar{v}_s . A linear least-squares regression is shown as the thick line and a perfect fit 1:1 line is shown dashed.

The fitted parameters are not statistically different from a linear regression with slope 1 and intercept 0, at the 95% significance level, as interpreted from an *f*-test (Bendat and Piersol, 1986).

A histogram of the error between the two measurements, given by the difference between the surface and interior currents, v_{diff} ,

$$v_{diff} = \bar{v}_s - \bar{v}_i \quad (29)$$

is plotted in Figure 3.10. The root-mean-square difference between each record,

$$v_{rms} = \left[\frac{1}{N} \sum v_{diff}^2 \right]^{\frac{1}{2}} \quad (30)$$

is 0.10 m/s, where *N* is the number of points being compared.

While the differences, v_{diff} , could be simply measurement or technique errors, they could also represent real differences between interior and surface currents. We first examined the relationship between alongshore wind stress and v_{diff} (Figure 3.11). The results for the full data set show a scattered relationship with a correlation of 0.58, which is significant, but not startling. However, partitioning of the data by wave angle revealed a surprising result. For waves arriving from the south ($\alpha < 0^\circ$), we found a good correlation ($r = 0.84$) between v_{diff} and alongshore wind stress, while in the cases where the peak energy waves are arriving from north ($\alpha > 0^\circ$) the differences are scattered with no discernible

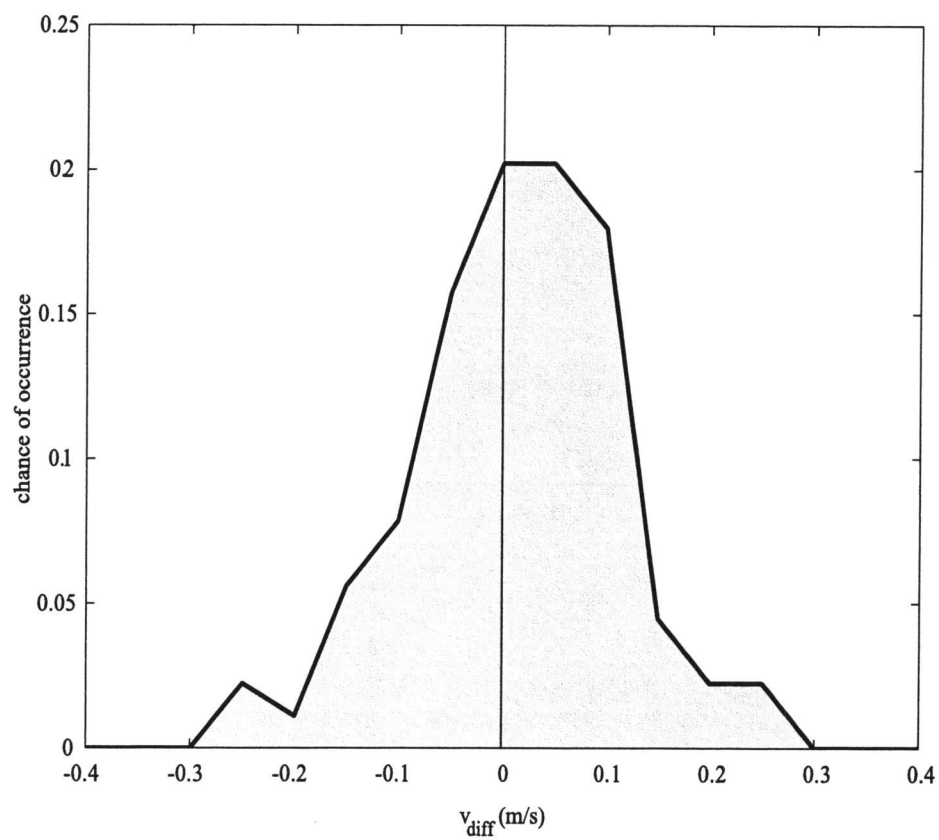


Figure 3.10 Probability density plot of the difference between mean surface and interior longshore currents, v_{diff} .

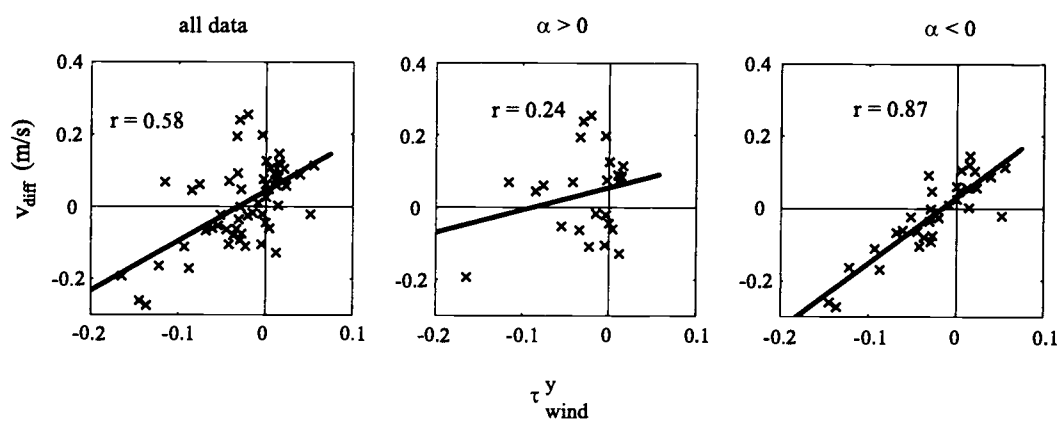


Figure 3.11 v_{diff} compared to the alongshore component of wind stress. All of the data is plotted in the left panel, the middle panel is the data for cases when the peak wave direction from the north, and the right panel shows data for the peak wave direction from the south. Linear least squares regressions and correlations are plotted in each panel.

relationship to wind stress ($r = 0.24$).

The relationship of v_{diff} to alongshore directed roller stress was also examined. We calculated the alongshore component of roller stress (Dally and Brown, 1995) using the cross-sectional area representation of the roller by Svendsen (1984)

$$\tau_{roller}^y = \rho_r g 0.9 H_0^2 \sin(\beta_s) \sin(\alpha). \quad (31)$$

The roller density, ρ_r , used here is 100 kg/m^3 , and H_0 is the significant wave height or $4\sigma_\eta$. Results were contrary to those in comparing v_{diff} to wind stress. In general the relationship between roller stress and v_{diff} is very scattered (Figure 3.12; $r = 0.07$). Contrary to wind stress, for cases when $\alpha < 0^\circ$ we find a slightly decreased, and not statistically significant at the 95% acceptance level, correlation ($r = 0.04$) of v_{diff} to roller stress than when $\alpha > 0^\circ$ ($r = 0.25$). While this is significant, it is not an illuminating correlation, due to the large degree of scatter.

3.5 Analysis of Vertical Shear in the Upper Water Column

Field tests have shown that the optical method to measure longshore currents produced surface velocity estimates with an effective gain of 100%. While we expected that there should be little difference between the two estimates since the water column was well mixed by turbulent dissipation due to breaking waves, it is possible that the differences that could represent real vertical shear, not measurement error. Three potential process-based sources of discrepancy may be

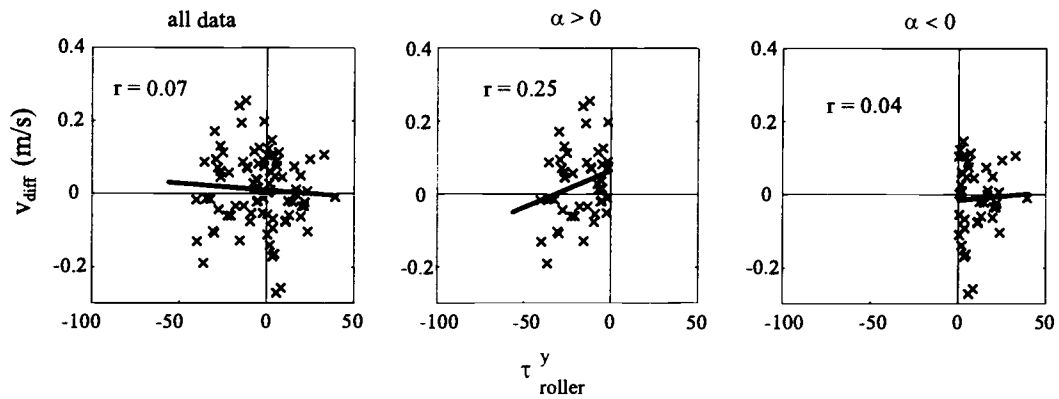


Figure 3.12 v_{diff} compared to the estimated alongshore component of wave roller stress. In the left panel all the data is plotted, in the middle panel is the data for cases when the peak wave direction from the north, and the right panel shows data for the peak wave direction from the south. Linear least squares regressions and correlations are plotted in each panel.

the cause, vertical shear due to a log boundary layer, shear due to surface wind forcing and shear due to a surface roller stress, though we explore the effect of viewing geometry as the probable source of error.

A mean longshore current, flowing over the bottom, will develop a shear profile described by a logarithmic boundary layer (Monin and Yaglom, 1975). Since we only have a surface measurement and one in the interior we cannot diagnostically test for a log-layer. However, we believe that vertical shear in the upper portion of the water column will be small due to boundary layer effects, on the order of a few cm/s (e.g. Garcez Faria *et al.*, 1998). The magnitudes of the differences we have measured in this experiment ranged from near zero to about 0.3 m/s and the root-mean-square error was 0.10 m/s. The log-layer model also predicts the surface velocity to be the same sign and larger in magnitude than the interior current. Instead, our gain is 1.0 and there are cases in which the discrepancy is of either sign (Figure 3.9). Comparisons of the alongshore component of roller stress to longshore velocity discrepancies v_{diff} reveal a very scattered between the two, therefore we don't consider roller stress a probable source of the discrepancies.

An alongshore component of wind stress would also drive a surface boundary layer, with surface longshore velocity shear in the same direction and with a magnitude that varied with the alongshore component of wind stress. Comparison of the differences between the surface and interior currents and

τ_y^{wind} showed a positive correlation to wind stress, that was significant but substantially improved by examining only instances for which the wave direction was from the south of the normal to shore (Figure 3.10).

The difference in the relationship as compared to wave direction could be due to the effect of the Field Research Facility pier. The pier is about 200 m south of the location of the current meters and extends 500 m from the shoreline. The pier may have a screening effect on waves and winds approaching from the south. If winds alone were screened, resulting in an actual wind stress that was less than the calculated wind stress, we would have observed reduced correlations when winds were from the south, but we see an increased correlation.

Finally, the most probable cause of the error is likely due to misregistration issues in the OCM method. As explained in section 2.2.6, we correct errors in the raw OCM estimates due to the fact we view a moving surface caused by waves. This correction depends on wave height, period, angle and the relative positions of the OCM pixel array and the location of the camera. While our assumption of a monochromatic sawtooth wave field allowed us to analytically determine a correction, it may have oversimplified the problem. Particularly, we assumed that the surface longshore current signal (advecting foam patches) would be confined to the falling portion of the wave, not the wave face. Due to the geometry of the situation, we may indeed see the backs of the waves more frequently as the waves

are coming from the south, appropriate to our model. However, for waves approaching directly in the angle for which we were viewing we see wave faces more frequently, inconsistent with our model. So, while we see a scattered relationship with surface velocity shear and alongshore wind stress for waves from the north we believe we have captured wind induced surface velocity shear, for cases when our $v_{apparent}$ correction model was valid.

Chapter 4: Discussion

While the Optical Current Meter performs very well it does have the requirement of additional data (wave height, angle and period) to get an accurate estimate of longshore currents. In cases where this information is at hand a correction to the raw estimate $v_{apparent}$ using equation (23) is easily calculated. For the camera arrangement at Duck, NC used in the field experiment, monochromatic waves with period 10 s and 1 m height will cause an apparent velocity of nearly 0.3 m/s, decreasing the wave height by half halves the apparent velocity. To avoid having to make the correction for misregistration at all, the optimal arrangement is to position the OCM array directly offshore of the camera.

The Optical Current Meter will be particularly useful in longshore current monitoring and large scale coastal behavior studies, and in specific scientific applications. The main reasons for this are the easy set up and deployment of an optical current meter, the ability to change and adapt the placement of an optical current meter to changing conditions (e.g. changing bathymetry or wave conditions), the ability to deploy multiple OCM arrays simultaneously in a variety of configurations, and the long term (years) measurements capability made possible from the long lived camera stations on which the OCM relies.

The main application of the OCM will be to measure and monitor longshore

currents to estimate alongshore sediment transport as a driving factor in sediment transport models, and to verify nearshore fluid dynamic models. This will be important in applications such as predicting erosion and accretion rates of beach sediment, analyzing the impact of structures like jetties and piers on sediment transport, and in analyzing the flow field in the vicinity of beach nourishments and inlets. Even though longshore currents have a direct role in beach behavior few, if any, longshore current records exist that have sufficient length and spatial coverage to do these analyses. An extension of this will be to use OCMs on a larger scale to describe the dynamics of large scale coastal behavior (LSCB), that is, patterns of beach variance over large spatial scales, hundreds of meters to kilometers, and over time scales of weeks to years.

Many arrangements of OCMs, such as a grid of arrays used to measure longshore currents over a two-dimensional field, could be used to analyze possible sediment transport patterns and to test nearshore circulation models. Another setup, that could be used for long term monitoring, may simply include a cross-shore array of optical current meters used to measure the cross-shore profile of the longshore current. An example of such an array was tested at Duck NC in the fall of 2001. The array consisted of 7 individual optical arrays spaced 20 m apart and spanning 140 m across the surf zone (Figure 4.1).

Optical current meters could also be useful in studying shear waves, a newly

Cross-shore OCM Array at Duck, NC

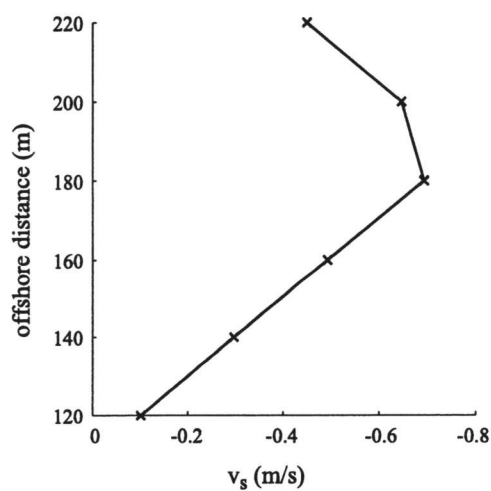
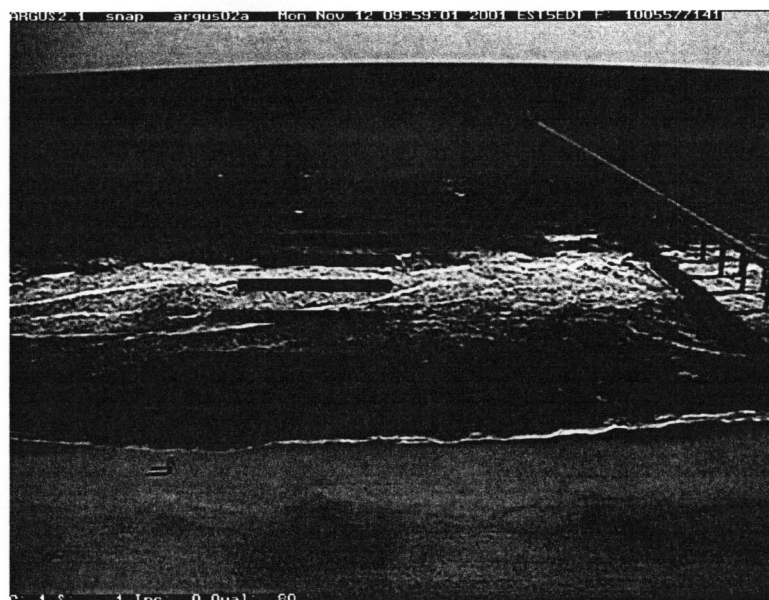


Figure 4.1 A cross-shore OCM array designed to measure the mean cross-shore profile of the longshore current (upper panel). In the lower panel a three hour mean current profile shows a current peak in the surf zone at about the break point.

described type of motion in the surf zone associated with longshore current instabilities. Shear waves are low frequency (< 0.01 Hz) progressive oscillations in the longshore current, with wavelengths on the order of 100 m (Oltman-Shay et al., 1989). Unlike motions of similar frequency, such as edge waves, these oscillations are non-dispersive. The dynamics of shear waves were first proposed by Bowen and Holman (1989) as a shear instability of a steady longshore current. Further modeling of these shear instabilities has shown that they may at times exhibit a chaotic and turbulent nature, shedding vortices offshore (Özkan-Haller, 1996).

Besides providing a more complete understanding of longshore current dynamics, shear wave kinematics have a direct effect on the distribution momentum in the surf zone by affecting mixing in the cross-shore direction. This can alter the mean cross-shore profile of the longshore current, and in turn affect the pattern and degree of the alongshore transport of beach sediments. Only a handful of observations of shear waves on two beaches (during the 1980 NSTS experiment at Leadbetter Beach in southern California, and at the 1986 SUPERDUCK experiment at Duck, North Carolina) are published (Oltman-Shay *et al.*, 1989; Dodd *et al.*, 1992). Many questions remain concerning the turbulent or wave-like nature of shear waves and how or if shear waves are manifested on other beaches.

A test application of the OCM to measure shear waves at Duck was performed in November 2001. Three hour records of longshore currents were

measured from a seven element alongshore array of Optical Current Meters, designed specifically to measure shear wave motions (Figure 4.2). An iterative maximum likelihood estimate (Pawka, 1983) of the frequency- wavenumber spectrum from data taken on November 12, 2001 showed substantial energy in the expected shear wave energy region of the spectrum.

Longshore OCM Shear Wave Array in Cameras 3 and 1

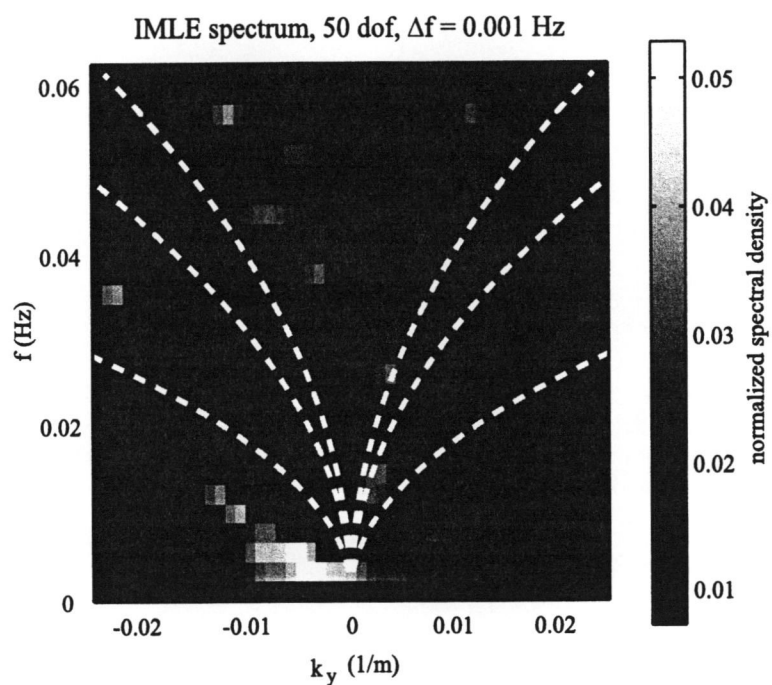
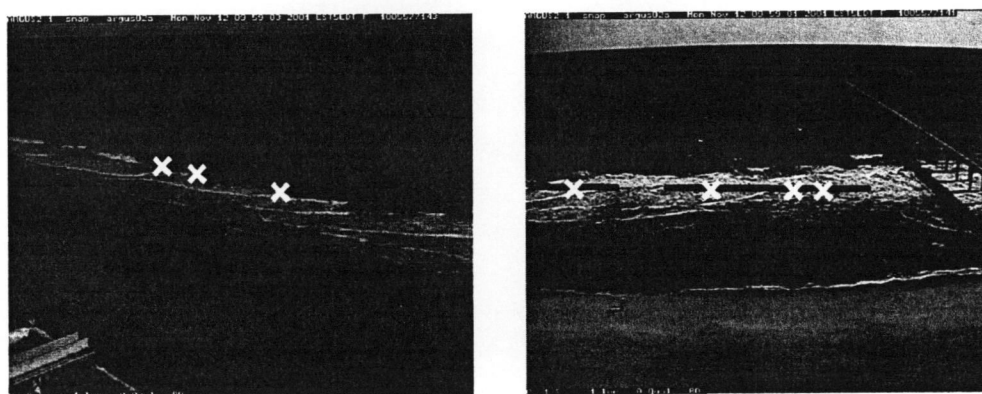


Figure 4.2 IMLE spectrum (lower panel) produced from a three hour record of longshore current velocity from the shear wave array (top panels). Energy concentration in the lower frequencies is associated with southward propagating shear waves. Also plotted are the estimated dispersion curves for 0, 1 and 2 mode edge waves.

Chapter 5: Conclusions

We have developed a method to measure surface longshore current time series in the surf zone through optical imaging of the alongshore drift of persistent sea foam, a technique called Optical Current Meter or OCM. In contrast to patch-based foam tracking techniques, this approach uses time series data from only an alongshore oriented transect of pixels. The space-time data are then Fourier transformed to a frequency-wavenumber spectrum, then transformed to a velocity spectrum, and finally fitted to a non-linear model based on the advecting foam signature. The method returns 95% confidence limits on velocity estimates, and a measure of the quality of the input video data.

Tests of the OCM, performed with synthetic data, indicate this method accurately estimates the mean current (with a maximum RMS error of 0.033 m/s) for a range of mean velocities (0 to 1.5 m/s), a range of contaminating wave motions (maximum longshore component of wave orbital velocities from 0 to 0.5 m/s), and a range of window lengths (8, 16, 32, 64 and 128 s). An optimal size window (32 s) was found to have small errors (RMS error = 0.012 m/s) while maintaining good resolution of low frequency motions, and is recommended for any further implementation of the OCM.

A field test conducted with data from Duck, NC showed mean longshore

surface currents measured with the OCM correspond closely to mean currents measured from a collocated in situ current meter (RMS error of 0.10 m/s) with a gain between the two measurements not statistically different from one. Those differences between mean surface and interior currents that did exist correlated well to the alongshore component of local wind stress ($r = 0.84$) for cases when our optical current measurements were correctly adjusted. We found that an estimate for the alongshore component of wave roller stress did not have a observable relationship to vertical shear in longshore currents during SandyDuck. While not conclusive, this first ever examination of surface current shear may lead to the development of a more complete model of the vertical structure of the longshore current including an improved understanding of the role of wind stress in longshore current dynamics.

The OCM will be invaluable in increasing the database of longshore current measurements. This will produce data to enhance large-scale coastal behavior studies providing a guess on likely alongshore sediment transport caused by longshore currents, and provide an engineering tool to monitor the alongshore flow field around natural and man-made structures. Additionally, OCM measurements of longshore currents will increase the range of environmental conditions, especially at beaches with complex bathymetry, with which to test nearshore models of fluid dynamics and sediment transport. A more specific application will

be to measure the relatively recently discovered shear waves, low-frequency motions in the longshore current. Non-linear shear wave models detailing turbulent motions have been developed, but not verified due to the lack of data.

Bibliography

Bendat, J.S., and A.G. Piersol, *Random Data Analysis and Measurement Procedures*, John Wiley & Sons, New York, 566 pp., 1986.

Birkemeier, W.A., H.C. Miller, S.D. Wilhelm, A.E. DeWall, and C.S. Gorbics, *A User's Guide to the Coastal Engineering Research Centers (CERC's) Field Research Facility*, miscellaneous Report, CERC-85-1, United States Army Engineer Waterways Experiment Station, 136 pp., 1985.

Birkemeier, W.A., C. Donoghue, C.E. Long, K.K. Hathaway, and C.F. Baron, *1990 DELILAH Nearshore Experiment: Summary Report*, Technical Report CHL-97-24, U.S. Army Corps of Engineers Waterways Experiment Station, 213 pp., 1997.

Birkemeier, W.A., C.E. Long, and K.K. Hathaway, DELILAH, DUCK94 & SandyDuck: three nearshore field experiments, *Proceedings of the 25th International Conference on Coastal Engineering*, Orlando, FL, American Society of Civil Engineers, 4052-4065, 1996.

Bowen, A.J., The generation of longshore currents on a plane beach, *Journal of Marine Research*, 27(2), 206-215, 1969a.

Bowen, A.J., Rip currents, 1, theoretical investigations, *Journal of Geophysical Research*, 74(23), 5467-5478, 1969b.

Bowen, A.J., D.L. Inman and V.P. Simmons, Wave "set-down" and wave set-up, *Journal of Geophysical Research*, 74, 2569-2577, 1968.

Bowen, A.J., and R.A. Holman, Shear instabilities of the mean longshore current 1. theory, *Journal of Geophysical Research*, 94(12), 18023-18030, 1989.

Chruch, C.C., E.B. Thornton, and J. Oltman-Shay, Mixing by shear instabilities of the longshore current, *Proceedings of the 23rd International Conference on Coastal Engineering*, Venice, Italy, 2999-3011, 1992.

Corps of Engineers, *Shore Management Guidelines: National Shoreline Study*, Washington D.C., U.S. Army Corps of Engineers, 56pp., 1971.

Dally, W.R., and C.A. Brown, A modeling investigation of the breaking wave roller with application to cross-shore currents, *Journal of Geophysical Research*, 100(12), 24873-24883, 1995.

Dean, G.R., and R.A. Dalrymple, *Water Wave Mechanics for Engineers and Scientists*, Prentice-Hall, New Jersey, 353 pp., 1984.

Dodd, N., J. Oltman-Shay and E.B. Thornton, Shear instabilities in the longshore current: a comparison of observation and theory, *Journal of Physical Oceanography*, 22, 62-82, 1992.

Elgar, S., R.T. Guza, W.C. O'Reilly, B. Raubenheimer, and T.H.C. Herbers, Wave energy and direction observed near a pier, *Journal of Waterway, Port, Coastal, and Ocean Engineering*, 127(1), 2-6, 2001.

Fedderson, F., R.T. Guza, S. Elgar, T.H.C. Herbers, Alongshore momentum balances in the nearshore, *Journal of Geophysical Research*, 103(8), 15667-15676, 1998.

Garcez Faria, A.F., E.B. Thornton, T.P. Stanton, C.V. Soares and T.C. Lippmann, Vertical profiles of longshore currents and related bed shear stress and bottom roughness, *Journal of Geophysical Research*, 103(2), 3217-3232, 1998.

Goss, H., Beach renourishment: the lessons of one Long Island community, *Coastal Services*, 5(4), 4-9, 2002.

Guza, R.T., and E.B. Thornton, Local and shoal comparisons of sea surface elevations, pressures and velocities, *Journal of Geophysical Research*, 85(3), 1524-1530, 1980.

Holland, K.T., and R.A. Holman, The statistical distribution of swash maxima on natural beaches, *Journal of Geophysical Research*, 98(6), 10271-10278, 1993.

Holland, K.T., R.A. Holman, T.C. Lippmann, J. Stanley and N. Plant, Practical use of video imagery in nearshore oceanographic field studies, *IEEE Journal of Oceanic Engineering*, 81-92, 1997.

Holman, R.A., A.H. Sallenger, Jr., T.C. Lippmann and J.W. Haines, The application of video image processing to the study of nearshore processes, *Oceanography*, 6(3), 78-85, 1993.

Jenkins, G.M., and D.G. Watts, *Spectral Analysis and its Applications*, Holden-Day, 1968.

Komar, P.D, *Beach Processes and Sedimentation*, Prentice-Hall, New Jersey, 544 pp., 1998.

Large, W.G. and S. Pond, Open ocean momentum flux measurements in moderate to strong winds, *Journal of Physical Oceanography*, 11, 324-336, 1981.

Lippman, T.C, and R.A. Holman, Phase speed and angle of breaking waves measured with video techniques, *Proceedings of a Specialty Conference of Coastal Sediments, '91*, Seattle, WA, American Societies of Civil Engineers, 542-556, 1991.

Long, C.E., and J.M. Oltman-Shay, *Directional characteristics of waves in shallow water*, Technical Report CERC-91-1, U.S. Army Engineers Waterways Experiment Station, 129 pp., 1991

Longuet-Higgins, Longshore currents generated by obliquely incident sea waves, 1, *Journal of Geophysical Research*, 75(33), 6778-6789, 1970a.

Longuet-Higgins, Longshore currents generated by obliquely incident sea waves, 2, *Journal of Geophysical Research*, 75(33), 6790-6801, 1970b.

Longuet-Higgins, M.S. and R.W. Stewart, Radiation stresses in water waves: A physical discussion, with applications, *Deep-Sea Research*, 11, 529-562, 1964.

Mei, C.C., *The Applied Dynamics of Ocean Surface Waves*, World Scientific Publishing, New Jersey, 740 pp., 1989.

Monin, A.S. and A.M. Yaglom, *Statistical Fluid Mechanics: Mechanics of Turbulence*, vol. 2, MIT Press, Cambridge, Massachusetts, 874 pp., 1975.

Munk, W.H., On the wind-driven ocean circulation, *Journal of Meteorology*, 7, 79-93, 1950.

Oltman-Shay, J., P.A. Howd and W.A. Birkemeier, Shear instabilities of the mean longshore current 2. field observations, *Journal of Geophysical Research*, 94(12), 18031-18042, 1989.

Özkan-Haller, H.T., and J.T. Kirby, Numerical study of low frequency surf zone motions, *Proceeding of the 25th International Conference on Coastal Engineering*, 1361-1374, 1996.

Özkan-Haller, H.T., and J.T. Kirby, Shear instabilities of longshore currents: flow characteristics and momentum mixing during SUPERDUCK, *Proceedings of the 3rd Coastal Dynamics Conference 1997*, 466-475, 1997.

Pawka, S.S., Island shadows in wave directional spectra, *Journal of Geophysical Research*, 88, 2579-2591, 1983.

Plant, N.G., R.A. Holman, M.H. Freilich, and W.A. Birkemeier, A simple model for interannual sandbar behavior, *Journal of Geophysical Research*, 104(7), 15755-15776, 1999.

Press, H.W., S.A. Teukolsky, W.T. Vetterling and B.P. Flannery, *Numerical Recipes in C The Art of Scientific Computing Second Edition*, Cambridge university Press, Cambridge, 994 pp., 1992.

Putrevu, U.J., J. Oltman-Shay, and I.A. Svendsen, Effect of alongshore nonuniformities on longshore current predictions, 100(8), 16119-16130, 1995.

Reniers, A., Longshore Current Dynamics, Delft Technical University, Ph.D. thesis, 133 pp., 1999.

Symonds, G. and D.A. Huntley, Waves and Currents over Nearshore Bar Systems, *Proceedings of the Canadian Coastal Conference*, 64-78, 1980.

Taylor, G.I., Skin friction of the wind on the Earth's surface, *Proceedings of the Royal Society of London*, A92, 196-199, 1916.

Thornton, E.B., and R.T. Guza, Transformation of wave Height Distribution, *Journal of Geophysical Research*, 88(10), 1983.

Thornton, E.B., and R.T. Guza, Surf zone longshore currents and random waves: field data and models, *Journal of Geophysical Research*, 16(7), 1165-1178, 1986.

Whitford, D.J., and E.B. Thornton, Comparison of wind and wave forcing of longshore currents, *Continental Shelf Research*, 13(11), 1205-1218, 1993.

Wolf, P.R. and B.A. Dewitt, *Elements of Photogrammetry: With Applications in GIS*, McGraw-Hill, Boston, 608 pp., 2000.

Wright, L.D., and A.D. Short, Morphodynamics of beaches and surf zones in Australia, *CRC Handbook of Coastal Processes and Erosion*, P. Komar (ed.), 35-64, 1983.